Thermal properties of lattice defects formed in ZnO and their contribution to n-type conduction

Doctoral thesis

Thermal properties of lattice defects formed in ZnO and their contribution to *n*-type conduction

Division of Material Chemistry
Graduate School of Natural Science and Technology
Kanazawa University

Student ID Number 1724022001
Name Hiromichi Shimizu
Chief Supervisor Professor Wataru Sato
Filing Date January, 2020

Contents

Abstract

Zinc oxide (ZnO) has received expectation as an alternative material replacing semiconductors which can be applied to electric devices being essential in the modern society. For the application of ZnO, intrinsic *n*-type conduction has been known to be a very important physical property of the material. Although interstitial zinc atoms (Zn_i), oxygen vacancies (V_O), and impurity hydrogen atoms (H) generated or incorporated in the matrix during the crystal growth processes and heat treatments are regarded as the origin of the conduction, the mechanism of carrier generation is still not clearly understood. Accordingly, it is of great importance to obtain information on the physical and/or chemical state and thermal behavior of lattice defects contributing to the *n*-type conduction of the undoped ZnO. In order to reveal the origin of the conduction, in this work, $^{1}H(^{15}N,\alpha\gamma)^{12}C$ nuclear reaction analysis (NRA), positron annihilation lifetime spectrometry (PALS), and electric conductivity measurements were performed to investigate their state of being in hydrothermally grown ZnO single crystals.

The NRA results suggest that H in the as-grown sample take three different bound states: two types are loosely bound to the lattice (LBH1 and LBH2) and the other is a strongly bound H (SBH). It is found that LBH1 and LBH2 are removed out of the nuclear reaction sites at 393 K and 773 K, respectively, but SBH survive with their average concentration of 0.10(3) at.% even at 973 K. Compared with the PALS results and theoretical calculations, it is suggested that SBH exist as (zinc vacancy)-H complexes. The electric conductivity increases at 393 K but decreases stepwisely in the temperature range of 473-973 K; this tendency demonstrates that the electric conductivity does not simply correlate with the concentration of H.

The electric conductivity of the ZnO samples increases dramatically with rise in the heat-treatment temperature up to 1473 K, which indicates that intrinsic lattice defects

are formed. From the electric conductivity measurements with the photoexcitation and thermal excitation, the electric conduction originated from shallow (Zn_i) and deep donors (V_O) was observed in the samples heat-treated at 1073-1273 K. At 1373 K, however, the conductivity increased only when the sample was thermally excited, signifying that V_O become inactive electrically but only Zn_i contribute to the conduction. From the observed variation of the conductivity in the samples heat-treated under different oxygen partial pressures, the author proposes a new conduction mechanism that free electrons are generated from Zn_i through charge cancellation between zinc vacancies (V_{Zn}) and V_O when Zn_i and V_{Zn} are formed simultaneously in the presence of V_O.

Chapter 1 Introduction

Our life is filled with a variety of electronic devices which are essential in the modern society. They are composed of different materials such as metals, semiconductors, and insulators. Recently, depletion of rare resources has drawn considerable attention as a serious problem for their mass production, and various measures are taken against the problem. For example, indium tin oxide (ITO) is applied to transparent electrodes for the displays of smart phones and tablet personal computers, for example, which can replace keyboards as contact sensors. Its versatility has also reached the applications to functional devices such as solar cells and thin film transistors [1,2]. ITO, synthesized by doping In_2O_3 with a small amount of SnO_2, has a wide band gap of 3.75 eV and shows *n*-type electric conduction [3]. However, it is necessary to resolve the depletion of In resource which is reported to be as low as 50 ppb in the crust of the earth [4]. Recently, zinc oxide (ZnO) with a wide band gap of 3.4 eV has received high expectations as an alternative material to ITO because of relatively rich abundance of Zn (70 ppm) and its easy conversion to the *n*-type conduction by Al or Ga doping [5-9]. Apart from the impurity doping, it has been known that even undoped ZnO shows the *n*-type conduction since the beginning of semiconductor studies for ZnO in mid-1950s, although the origin of the conduction is still not clearly understood [10,11]. If the mechanism of the intrinsic *n*-type conduction is clarified and methods for precise control of the conductivity of the compound are established, supply of much cheaper devices would be realized because the donor doping processes become unnecessary. It is of great importance to investigate the origin of the *n*-type conduction of ZnO from a microscopic point of view because atom-level phenomena such as the formation and deformation of lattice defects and their interactions give rise to such bulk physical properties. The objective of this work is to clarify the mechanism of the defect-induced

n-type conduction based on the investigation of the formation and deformation processes of lattice defects and their thermal behaviors by means of radiation detection techniques sensitive to dilute defects and impurities.

1.1 Zinc oxide

Zinc oxide (ZnO) is a compound semiconductor having a hexagonal wurtzite structure, in which one cation (anion) is located in the center of the tetrahedron with four anions (cations) at each vertex of the tetrahedron as shown in Fig. 1. Table 1 shows the physical properties of ZnO [12,13].

ZnO is industrially produced by calcination of metal Zn in air or thermal decomposition of zinc sulfate and zinc nitrate. In recent years, the crystal growth methods such as the hydrothermal growth method are developed and high-quality single crystal ZnO has become easily available [14]. The single crystal of ZnO is transparent due to its band gap of 3.4 eV (Fig. 2). For ideal materials having a wide band gap, the concentration of free carriers in their conduction band is not high enough to contribute to the electric conductivity. However, lattice defects with a certain concentration exist in real materials because of the imperfection of the crystal. For undoped ZnO, it is considered that the *n*-type conduction is caused by the lattice defects generated during the crystal growth processes and heat treatments. As is described below, oxygen vacancies, interstitial zinc atoms, and impurity hydrogen atoms are considered as the candidates of the origin of the intrinsic *n*-type conduction [15-18].

1.2 Lattice defects in ZnO and their behaviors

Lattice defects are classified into the following three groups which deviate from

repeated spatial patterns in crystals: (1) atoms located in interstitial sites in the crystal, (2) atomic vacancies formed by desorption of lattice atoms existing in lattice points, (3) impurity elements intentionally introduced into the matrix to control its physical properties or unwantedly involved during the crystal growth processes. For the applications of ZnO in a variety of fields, it is essential to identify lattice defect species and control their state of being because lattice defects influence the physical and chemical properties of the matrix such as mechanical strength, electric conductivity, and chemical reactivity. In the following subsection, donor defects typical of ZnO are explained: oxygen vacancies, interstitial zinc atoms, and impurity hydrogen atoms.

1.2.1 Oxygen vacancy

It is well known that the number of Zn and O atoms is not stoichiometric: the number of oxygen atoms is generally somewhat less than that of zinc atoms. From this unbalance, it is easily expected that the lattice defects contributing to the *n*-type conduction are oxygen vacancies. Oxygen vacancy is a vacant lattice point formed by desorption of an oxygen atom as shown in Fig. 3(a) [19]. Using Kröger-Vink notion, the formation and ionization of oxygen vacancies can be described as follows [20].

$$O_O^{\times} \rightarrow V_O^{\times} + \frac{1}{2} O_2 \text{ (gas)}$$
$$V_O^{\times} \rightarrow V_O^{\bullet\bullet} + 2e'$$

Here, the superscript cross mark ($^{\times}$), superscript dot ($^{\bullet}$), and quotation mark ($'$) indicate the neutral, positive, and negative charge state, respectively, and the number of $^{\bullet}$ and $'$ shows the formal charge. *e* indicates the electron. The subscript symbol of elements means the lattice point of the indicated atoms. *V* indicates a vacancy meaning no atom in the indicated lattice point. From the above notions, it is found that oxygen vacancies

(V_O) are formed by desorption of lattice oxygen atoms (O_O) from their original lattice points and contribute as donors emitting two electrons [21]. According to the theoretical calculations [18,22], it is suggested that the defect level of V_O is formed at 2.0-2.5 eV below the conduction band. In some photoluminescence studies, a broad photoluminescence peak at 2.5 eV observed in ZnO samples is assigned to an emission originated from the electron transitions from the conduction band or its neighbor donor level to the level of V_O [23-25]. Donors having their levels far below the conduction band such as V_O are not regarded as the origin of the *n*-type conduction of the undoped ZnO because their electrons cannot be excited to the conduction band with thermal energy of room temperature (~25 meV); they are generally denominated deep donors.

1.2.2 Interstitial zinc atom

If the difference of the stoichiometric ratio of ZnO is attributed to the presence of excess zinc atoms but not to the existence of V_O, it is expected that the origin of the *n*-type conduction is interstitial zinc atoms. As shown in Fig. 3(b), interstitial zinc atoms are desorbed from their original lattice points to lie in the interstitial sites of ZnO lattice [19]. Using Kröger-Vink notion, the formation and ionization of interstitial zinc atoms can be described as follows [20].

$$Zn_{Zn}^{\times} \rightarrow Zn_i^{\times} + V_{Zn}^{\times}$$

$$Zn_i^{\times} \rightarrow Zn_i^{\bullet\bullet} + 2e'$$

Here, the elements with the subscript *i* lie in the interstitial sites. From the above notion, it is found that interstitial zinc atoms (Zn_i) are formed by desorption of lattice zinc atoms (Zn_{Zn}) leaving zinc vacancies (V_{Zn}) as the counterpart of the Frenkel pair of Zn_i. In the case of the formation of Zn_i with the neutral charge state, they emit two electrons to

convert to cations with the charge state of 2+. In a previous study, the lattice defects formed in ZnO single crystals by high-energy electron irradiation were identified as Zn_i, and their defect levels formed at 30 meV below the conduction band were close to that of donors existing in as-grown samples; therefore, it was suggested that Zn_i contribute to the conduction as main donors in the as-grown samples [26]. According to the above experimental fact and some theoretical calculations, Zn_i are classified as shallow donors because their electrons are transferred to the conduction band by thermal energy of room temperature. However, the concentration of Zn_i is not high enough to contribute to the *n*-type conduction because (1) their formation energy is high and (2) they easily escape out of the system due to their low diffusion energy in ZnO lattice [19].

Figure 3(c) shows zinc vacancies (V_{Zn}), which are surrounded by four oxygen atoms. In contrast to Zn_i, V_{Zn} are easily formed in *n*-type ZnO to trap excess free electrons as acceptors [19]. Using Kröger-Vink notion, the ionization of V_{Zn} can be described as follows.

$$V_{Zn}^{\times} \rightarrow V_{Zn}'' + 2h^{\bullet}$$

Here, *h* indicates the hole. V_{Zn} can emit two holes formally; however, it is considered that the *p*-type conduction is not induced even if only V_{Zn} are formed in ZnO because their defect levels are formed at a high level (~0.2 eV) above the valence band. It should be noted that electrons in donor levels such as V_O and Zn_i located higher than defect levels of V_{Zn} would be trapped by V_{Zn} to cancel out the electrons. Therefore, when Zn_i and V_{Zn} are generated simultaneously, Zn_i cannot contribute to the *n*-type conduction due to the charge cancellation with V_{Zn}.

1.2.3 Impurity hydrogen atoms

Impurity hydrogen atoms (H) exist in ZnO at a high concentration compared to any other impurity element involved during the crystal growth processes. The concentration of H is reported to be at least 0.3 at.% [27]. Their donor property is investigated experimentally in previous works. For example, muon spin rotation measurements revealed that positive muons, which behave as a light isotope of protons, trap electrons in ZnO below 40 K but release ones above the temperature, and the donor level of the positive muons are formed at 50-60 meV below the conduction band [28,29]. The result suggests that H behave as shallow donors.

In addition, a lot of theoretical and experimental works were performed for the states of H as described below [30-41]. As shown in Fig. 4, it is known that H can occupy different positions in ZnO lattice. Those shown in Fig. 4(a) are interstitial hydrogen atoms (H_i). Their formation energy is lower than those of the above native lattice defects, and H_i located on the Zn-O bonding perpendicular to the *c*-axis ($BC_{\perp}$) are the most stable among all H_i [30]. Using Kröger-Vink notion, the ionization of the interstitial hydrogen atoms can be described as follows.

$$H_i^{\times} \rightarrow H_i^{\bullet} + e'$$

According to the theoretical calculation [30], it is considered that the H_i take the charge state of 1+ to contribute to the *n*-type conduction. In an infrared spectroscopic study, the correlation between the concentration of free carriers in ZnO samples and the integrated peak area at 3611 cm^{-1} assignable to a local vibrational mode of an O-H bonding at $BC_{//}$ was shown [31], which implies that the hydrogen atoms of the O-H exist as donors in the ZnO samples. The ionization energy of H_i is estimated to be 53 meV by photoluminescence spectroscopy [33]. The above experimental reports suggest that

H_i would function as shallow donors in ZnO.

It is theoretically suggested that impurity hydrogen atoms substituting oxygen atoms (H_O) shown in Fig. 4(b) also behave as donors [37]. Using Kröger-Vink notion, the ionization of H_O can be described as follows.

$$H^{\times} + O_O{}^{\times} \rightarrow H_O{}^{\bullet} + \frac{1}{2} O_2 + e'$$

In the same way as H_i, it is considered that H_O take the charge state of 1+. It is theoretically suggested that the formation energy of H_O is comparable to that of H_i but H_O are thermally more stable than H_i [38]. The presence of H_O is recognized in some experiments [36,39,40]. In a nuclear magnetic resonance spectroscopic study, H_i and H_O can be distinguished by their chemical shifts and thermal behaviors [36]. However, there is no conclusive evidence for the contribution of H_O to the *n*-type conduction, and a theoretical calculation even suggests that H_O are not formed in ZnO [41]; it is still controversial whether H_O function as donor impurities in ZnO.

1.3 Applications of ZnO and its unavoidable *n*-type conduction

Much attention has been given to the wide band gap of ZnO, and there are various investigations for the applications of ZnO to photoelectric devices such as ultra violet detectors [42,43], solar cells [44,45], and light-emitting diodes [46-48]. In general, these devices have a junction structure with *n*-type and *p*-type semiconductors, and they are classified into two types: a hetero-junction and a homo-junction structures. The former is composed of different materials, and the latter the same materials. As shown in Fig. 5, in the case of the hetero-junction structure, dislocations are formed at the junction interface due to the difference of their lattice constants. In addition, one of the

joined materials peel off from the other at the interface as the concentration of dislocations increases. However, there is no lattice mismatch in the homo-junction structure because of the same lattice constants, and thus, homo-junction structures are preferable for the production of photoelectric devices.

Intrinsic semiconductors show insulator-like electric conduction because the concentration of free electrons or holes is very low. Doping of a small amount of impurity elements into the semiconductors increases the concentration of free carriers. For ZnO, the *n*-type conduction is realized by doping group 13 elements (Al, Ga) and group 17 elements (F, Cl) [49-53]. For the *p*-type conduction, ZnO is doped with alkali metal elements (Li, Na), group 11 elements (Cu, Ag), and a group 15 element (N) [54-59]. However, *n*-type conduction of undoped ZnO makes it difficult to produce *p*-type ZnO because the electrons inherent in ZnO matrix cancel out holes arising from the acceptors introduced into ZnO even at high acceptor concentration [60-62]. It is therefore important to clarify the origin of the unavoidable *n*-type conduction for the establishment of a methodology for the production of the *p*-type ZnO.

1.4 Objective of this work

Among the lattice defects described above, impurity hydrogen atoms are likely to be the most possible candidate bringing about the *n*-type conduction of undoped ZnO. However, it is reported that the electric conductivity and the free electron concentration in hydrothermally grown ZnO single crystals increase drastically as heat-treatment temperature is raised from 1173 K to 1473 K, which is higher compared with the desorption temperature of impurity hydrogen atoms (~973 K) [63]. This experimental fact implies that intrinsic donor defects (Zn_i and V_O) formed during the heat treatments contribute to the *n*-type conduction [64]. In addition, real samples include not only the

above donor defects but also acceptor defects such as V_{Zn}. A theoretical calculation for a net carrier concentration shows that the *n*-type conduction is brought about by the interaction among these defects; the idea that specific defects solely contribute to the conduction is not always true of real semiconductors including ZnO. Therefore, in order to clarify the origin of the *n*-type conduction, it is essential to identify defect species generated in ZnO and to understand their formation and desorption processes, thermal behaviors, and interactions in microscopic and macroscopic points of view.

The objective of this work is to reveal the mechanism of the *n*-type conduction induced by lattice defects generated in undoped ZnO. For the identification and determination of the defects, in this work, heat-treatment temperature dependences of the concentrations of the defects and electric conductivities were investigated for hydrothermally grown ZnO single crystals heat-treated at different temperatures by means of $^{1}H(^{15}N,\alpha\gamma)^{12}C$ nuclear reaction analysis, positron annihilation lifetime spectroscopy, and electric conductivity measurements. Based on all the results obtained, thermal behaviors and interactions of the defects are discussed, and a mechanism of the generation of carrier electrons in undoped ZnO is proposed.

1.5 Outline of this work

The present paper is composed of five chapters. The sample used in this work and the above experimental methods are explained in Chapter 2. The effect of H in ZnO on the *n*-type conduction is discussed in Chapter 3 based on the concentration and thermal behavior of H in hydrothermally grown ZnO single crystals. A mechanism of the generation of charge carriers from intrinsic defects such as Zn_i and V_O formed in the samples heat-treated at high temperature is proposed in Chapter 4. Finally, this work is summarized in Chapter 5.

Table 1 Physical properties of ZnO.

Space group	$P6_3mc$
Lattice constants at 300 K	
a	0.325 nm
c	0.512 nm
Ionic radii	
Zn^{2+}	60 pm
O^{2-}	138 pm
Density	5.606 g cm^{-3}
Molar weight	81.41 g mol^{-1}
Melting point	2248 K
Band gap	3.4 eV

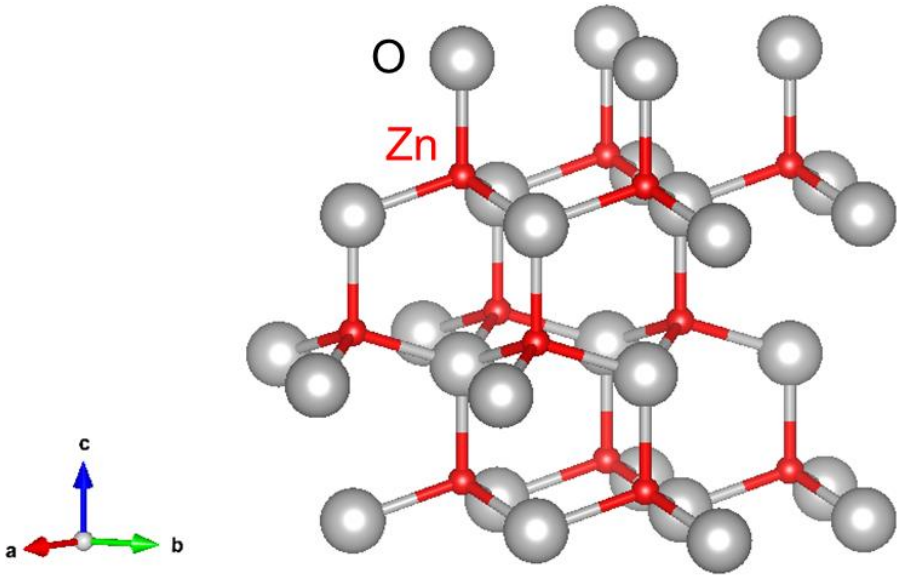

Fig. 1 Schematic illustration of the crystal structure of ZnO.

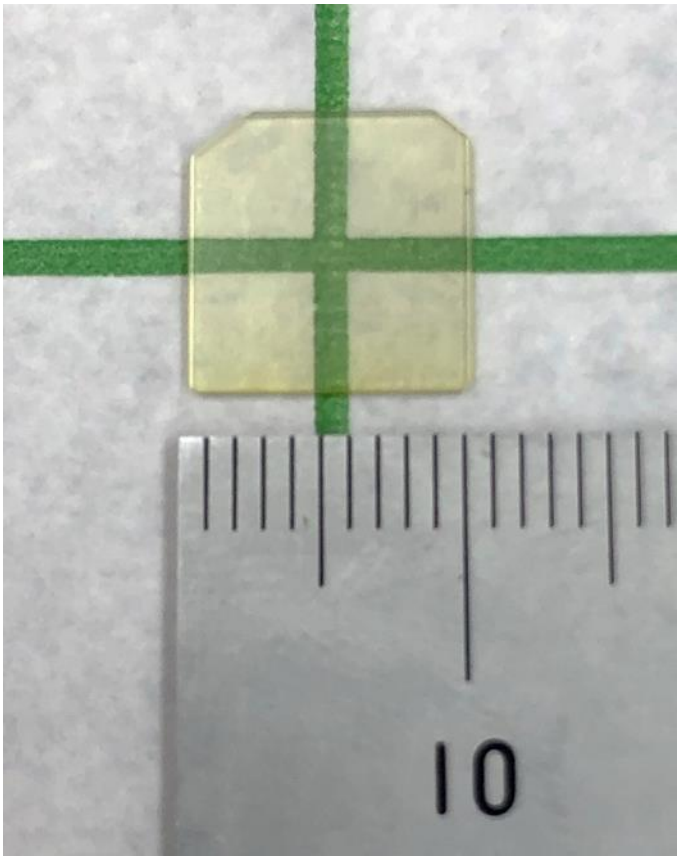

Fig. 2 Single crystal of ZnO.

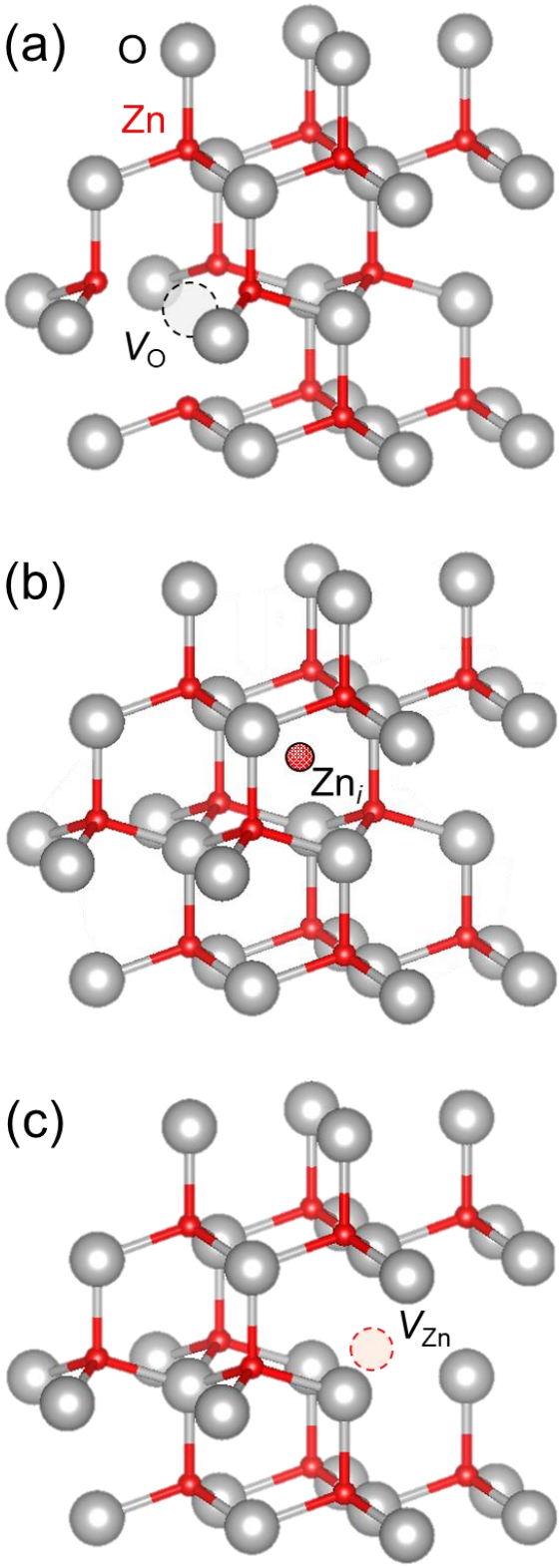

Fig. 3 Schematic illustrations of the crystal structure of ZnO. An oxygen vacancy, an interstitial zinc atom, and a zinc vacancy are shown in (a), (b), and (c), respectively.

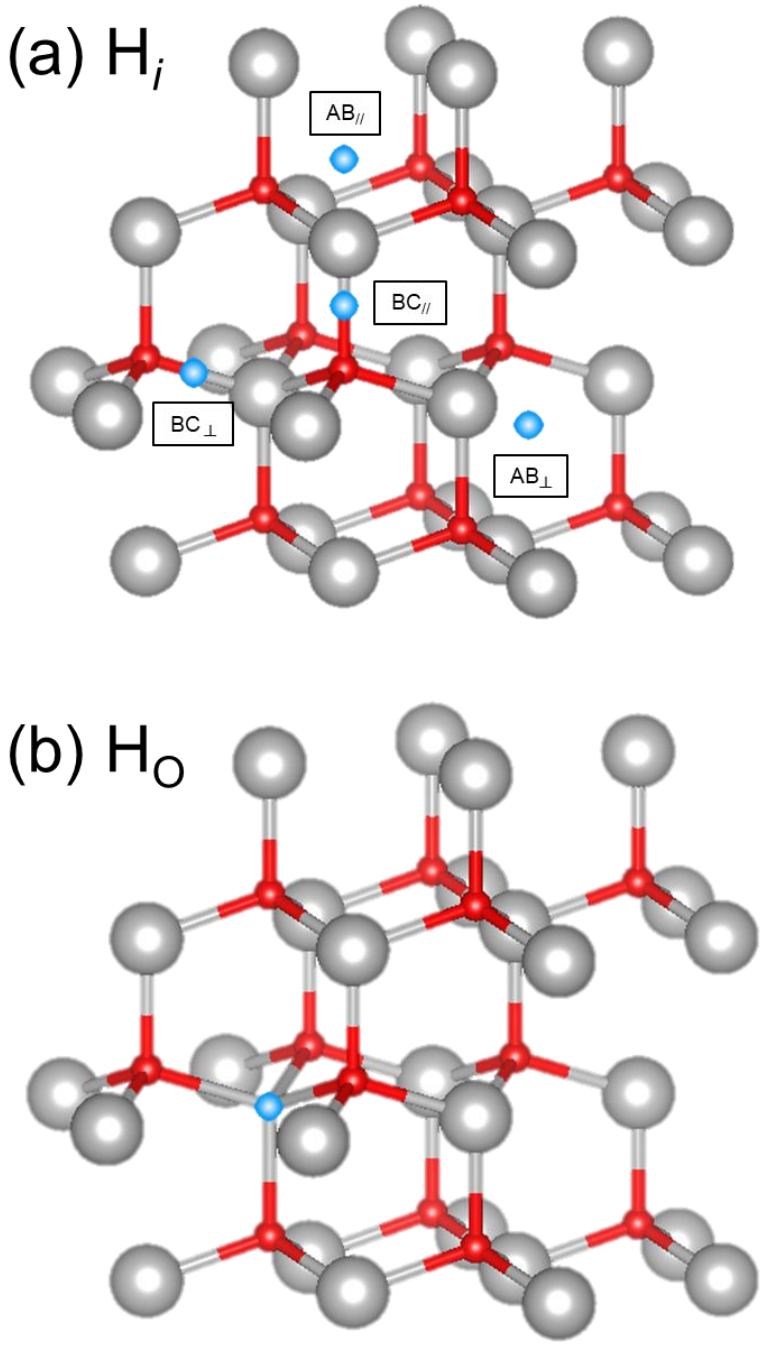

Fig. 4 Schematic configurations (a) of interstitial hydrogen atoms and (b) of a substituting hydrogen atom in ZnO. BC and AB indicate the bonding center site and anti-bonding site of oxygen atoms, respectively. // and ⊥ show bonding directions parallel and perpendicular to the *c*-axis of ZnO, respectively.

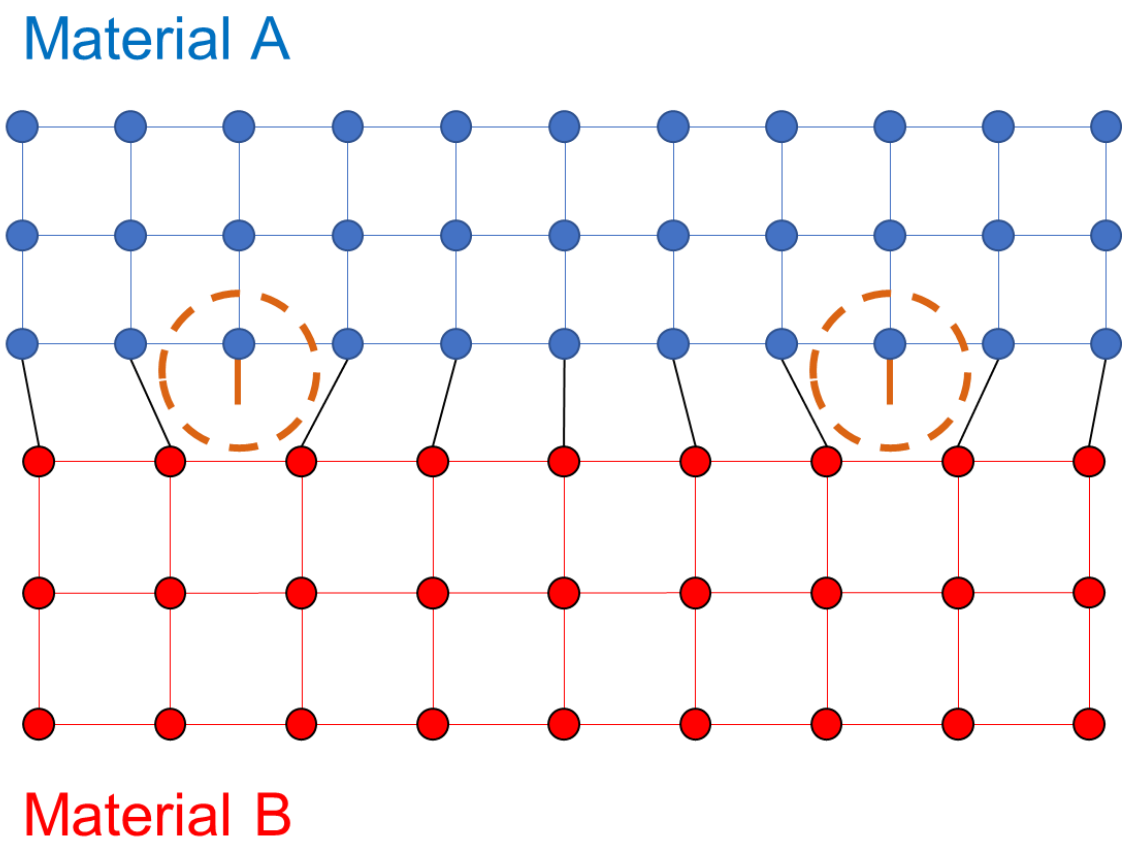

Fig. 5 Hetero-junction structure composed of Materials A and B having different lattice constants. Dislocations are formed in dotted circles.

Chapter 2 Experiments – Samples and Experimental methods

2.1 Hydrothermally grown ZnO single crystal

ZnO single crystals with a size of 10 × 10 × 0.5 mm^3 grown by the hydrothermal growth method (Optostar Ltd.) were used in this work (Fig. 2). Both surfaces of the samples were subjected to mirror polishing, and the plane orientations [0001] and [000-1] correspond to Zn- and O-face, respectively. The selling agency reports that their purity is above 99.97 at.% and the concentration of impurity elements such as Al, Cu, and Ti involved during the crystal growth processes is below 0.015 at.%. The agency also explains that electric resistivity of the samples is 10^4-10^5 Ω cm and reaches as high as ~10^8 Ω cm by heat treatments. In the case of powder samples and thin films, estimation of defects contributing to the conduction is difficult because there are a lot of grain boundaries causing the scattering of free charge carriers. On the other hand, single crystal samples have no grain boundaries; therefore, what affect the physical properties of single crystals are the presence and thermal behavior of the defects.

2.2 Determination of hydrogen atoms

The thermal behavior of deuterium (^{2}H) in ^{2}H-implanted ZnO samples was observed by means of secondary ion mass spectrometry (SIMS) [63]; however, the absolute concentration of ^{2}H in unknown samples cannot be determined unless an identical sample with known hydrogen concentration is prepared as a standard. In addition, the mass of ^{2}H is about twice as heavy as that of ^{1}H, which suggests that the isotope effect on their dynamic behavior is reflected clearly. Thus, even if the

information on ^{2}H is obtained, it cannot be said that the behavior of hydrogen atoms in the solid is elucidated exactly due to lack of information on that of ^{1}H.

In this work, nuclear reaction analysis (NRA) was employed to determine the absolute concentration of the impurity hydrogen atoms which are considered to contribute to the *n*-type conduction of the hydrothermally grown ZnO single crystals. In the NRA study, accelerated ions are implanted into the samples and the radiations arising from the nuclear reaction between the incident ions and target elements are detected to determine the concentration of the target elements. This method is suitable to determine dilute concentration of light elements such as H, Li, B, C, N, O, and F in solids [65]. In this section, the $^{1}H(^{15}N,\alpha\gamma)^{12}C$ nuclear reaction analysis and the experimental setup are described in detail.

2.2.1 $^{1}H(^{15}N,\alpha\gamma)^{12}C$ nuclear reaction analysis

There are very few methods highly sensitive for the determination of the absolute concentration of hydrogen atoms (nuclei), especially protons (^{1}H) in solids. This method was established by Lanford *et al*. in 1976 [66]. The nuclear reaction between ^{15}N and ^{1}H can be described as follows.

$$^{1}H + ^{15}N \rightarrow ^{12}C + \alpha + \gamma$$

4.43-MeV γ rays generated in the nuclear reaction are detected for the determination of the ^{1}H concentration. One of the main characteristics of the reaction is that a resonant nuclear reaction occurs when the kinetic energy of incident ^{15}N ions is 6.385 MeV [66]. The resonant nuclear reaction is a phenomenon that the reaction rate (cross section) increases remarkably when the kinetic energy of the incident ion matches the energy gap between an energy level of a compound nuclei formed by the nuclear reaction and a

potential energy of the incident ion and the target element. As shown in Fig. 6, the cross section for the resonant nuclear reaction reaches 1.65 b at the kinetic energy of the incident ^{15}N ions of 6.385 MeV [67]. It is possible to detect dilute hydrogen atoms with their concentration of ~0.01 at.% because of the extremely large cross section.

2.2.2 Experimental setup

The $^{1}H(^{15}N,\alpha\gamma)^{12}C$ NRA experiments were performed at BL-2C beam line in the MALT tandem accelerator facility of The University of Tokyo [68,69]. Figure 7 shows the schematic setup for the beam line. By spattering carbon-mixed $Ti^{15}N$ cathodes with Cs ions, $C^{15}N^{-}$ ions are recoiled out and accelerated by the tandem accelerator. On the way, the charge exchange of $C^{15}N^{-}$ ions is carried out in an Ar gas stripper to generate a $^{15}N^{q+}$ beam. After that, the beam passes through an energy analyzer, and the $^{15}N^{2+}$ beam is extracted and irradiated into the samples attached in a high vacuum chamber. As shown in Fig. 8, 4.43-MeV γ rays are detected using two bismuth germanate ($Bi_4Ge_3O_{12}$, BGO) scintillation detectors installed perpendicular to the beam direction outside the chamber. An anti-coincidence circuit combined with plastic scintillation detectors installed around the BGO detectors was used to reduce background signals of high-energy cosmic radiations. A background count rate in the energy range of the measured γ ray was 0.08(2) cps and was subtracted from all the data obtained in the present NRA experiments.

2.3 Positron annihilation lifetime spectrometry

Positron annihilation lifetime spectrometry (PALS) was performed to evaluate the states of isolated V_{Zn} and V_{Zn} complexes with impurity elements in the samples. In

this section, the property of positron, the principle of PALS, the experimental setup, the measurement method, and the data analysis are described in detail.

2.3.1 Positron

The existence of positrons was predicted by Dirac in 1930 [70] and was confirmed by using a cloud chamber with lead plates by Anderson in 1932 [71]. The positron is the antimatter of the electron, and the charge state of the positron is positive and its mass, electric charge, and spin are equal to those of the electron. Positrons annihilate with electrons of atoms, converting to photons. This phenomenon is called the positron annihilation. The number of emitted photons depends on the direction of the spins of the electrons annihilated with positrons. For an antiparallel spin direction between positrons and electrons (a singlet state), two photons are emitted in most cases. For a parallel spin direction (a triplet state), three photons are mainly emitted. The probability of the former is about 1115 times as high as that of the latter. In the center-of-mass system for the singlet state, two photons with an energy of 511 keV, corresponding to the rest mass of a positron or an electron, are emitted in the direction of 180° to each other.

In general, positrons are produced in the β^+-decay processes of radioisotopes or the pair-production processes. In the positron generation by the β^+-decay processes, proton-rich radioisotopes such as ^{18}F, ^{22}Na, and ^{68}Ga are used. The β^+-decay process can be described as follows.

$$p \rightarrow n + e^+ + \upsilon$$

Here, p, n, e^+, and υ indicate the proton, neutron, positron, and neutrino, respectively. The nucleus converts to the isobar having smaller atomic number by one through the process, for example $^{18}F \rightarrow {}^{18}O$.

2.3.2 Principle

Positron annihilation lifetime spectrometry (PALS) allows us to observe lattice defects, especially vacancy-type defects in materials at an atomic level, and thus plays an important role in the research fields of solid materials such as metals, semiconductors, and polymers.

In PALS measurements, the size and concentration of the vacancies are evaluated in nondestructive manner based on the time difference between the generation and annihilation of positrons [72]. In ideal single crystals, positrons occupy interstitial sites because they undergo electrostatic repulsion from nuclei in matter due to their positive charge. In real samples, positrons tend to be localized in the vacancy sites due to less repulsion compared to interstitial sites. For ionic crystals, cation vacancies take a relatively negative charge and attract positrons; however, anion vacancies refuse them. The probability of the collision of positrons with electrons in vacancies is small because the density of electrons in the site is lower than that at interstitial sites; therefore, positrons tend to survive in vacancies, and consequently, their lifetime become longer there. Positron lifetimes in metals and semiconductors are in the order of 10^{-10} seconds. On their surfaces and in polymers, however, positroniums (Ps) happen to be formed to annihilate with their lifetimes of 10^{-9}-10^{-8} seconds.

In the PALS method, radioisotopes such as the above nuclides or positron beams are used as positron sources. The former is more common and is employed in this work. ^{22}Na is the most common positron source. The decay scheme of ^{22}Na is shown in Fig. 9 [73]. There are three advantages in the use of ^{22}Na. The first advantage is its half-

life of 2.6 years, which allows a long-term usage. The second is the branching ratio for the β^+-decay process. The process always competes with the electron capture (EC) decay process. In the EC decay process, a 1s electron is captured by the nucleus to convert a proton to a neutron. In the case of ^{22}Na, because the probability of the β^+-decay process is 90%, positrons are predominantly emitted. The third is the half-life of the excited state of ^{22}Ne reached after the β^+-decay process. The excited state has a very short half-life of 3.6×10^{-12} seconds, and therefore a 1275-keV γ ray is emitted at almost the same time as the precedent emission of the β^+ particle; the timing when 1275-keV γ rays are emitted can be regard as that of the generation of positrons. The timings for the generation and annihilation of positrons are measured by the detection of a 1275-keV γ ray and a 511-keV photon arising from the positron annihilation, respectively.

2.3.3 Experimental setup

For the PALS measurement of the time difference of about 10^{-10} s between 1275-keV γ rays and 511-keV photons, in this work, an electric circuit equipped with barium fluoride (BaF_2) scintillation detectors was employed for the necessity of high time resolution. In the subsections below, the circuit and the source used in the present work are explained.

2.3.3.1 *Circuit*

The scheme of the electric circuit for the present PALS measurements is shown in Fig. 10. The circuit is composed of a variety of modules which are classified into two groups: (1) a time resolving circuit (solid lines) and (2) an energy selecting circuit (dashed lines). In the circuit (1), detected photons with the energies of 1275 and 511 keV as a start and a stop signals, respectively, are selected using the constant fraction discriminators (CFD), which output only electric signals exceeding the discrimination

levels. The time-to-amplitude converter (TAC) accepts these signals and produces an electric pulse with an amplitude proportional to the time interval between the signals to output to the analog-to-digital converter/ multi-channel analyzer (ADC/MCA). In order to record an overall view of a peak at time zero in the PALS spectrum, the output signal of the CFD was delayed for the stop signal side. In the circuit (2), signals arising from the two detected photons are discriminated at the single channel analyzers (SCA) based on their pulse heights after the amplification of the signals by the amplifiers (Amp.). Each output signal was put into the universal coincidence (UC) to confirm as identical events. A logic signal produced by the UC was sent to the gate and delay generator (GDG) and the output signal was put into the ADC/MCA as a gate signal. Only when the output timings for the signals from the circuit (1) and (2) coincide, the signals from the circuit (1) were output to the personal computer.

2.3.3.2 *Source*

Figure 11(a) shows the composition of the positron source used in this work. Droplets of hydrochloric acid solution of ^{22}Na was dropped on a Kapton film with a thickness of 7.5 μm and was dried up. Next, it was covered with another identical Kapton film, and finally, the Kapton films were sealed with Kapton tapes with a hole. The Kapton film and tape are composed of polyimides having a molecular structure shown in Fig. 12 and are a suitable source material because Ps are hardly formed in the Kapton films due to high electron affinity of a pyromellitic anhydride [74]. As shown in Fig. 11(b), the positron source was sandwiched with two identical samples in which positrons are stopped to annihilate with electrons.

2.3.4 Measurement method and data analysis

The PALS spectra were analyzed with a fitting program PALSfit in this work [75]. The PALS spectrum $N(t)$ is theoretically expressed as [72]

$$N(t) = \sum_{i=1}^{k+1} \frac{I_i}{\tau_i} \exp\left(-\frac{t}{\tau_i}\right) + \text{B. G.} \tag{1}$$

Here, τ_i and I_i indicate the positron lifetime and intensity for the component i and reflect the size and concentration of vacancies, respectively. k represents the expected number of vacancy species in the sample, and the total number of the annihilation sites is represented as $k + 1$ including the annihilation event in the bulk. It should be noted that it is difficult to decompose a spectrum into each component; therefore, the author obtained rough information on the vacancy species by decomposing a spectrum into two components of a shorter and a longer lifetimes. B. G. is the background counts arising from random coincidence events.

The PALS spectra are theoretically expressed by Eq. (1); however, the following equation is used practically because the real spectra include a Gaussian distribution originating from the time resolution of the measurement system.

$$N(t) = \left\{\sum_{i=1}^{k+1} \frac{I_i}{\tau_i} \exp\left(-\frac{t}{\tau_i}\right)\right\} * \sum_{j=1} \left[\frac{I_j}{\sqrt{2\pi\sigma_j^2}} \exp\left\{-\frac{(t - t_0)^2}{2\sigma_j^2}\right\}\right] + \text{B. G.} \tag{2}$$

Here, the second summation operator indicates the Gaussian function and the symbol $(*)$ stands for the convolution integration. σ and t_0 indicate the distribution and central value

of the Gaussian function, respectively. The time resolution is represented as a full width at half maximum (FWHM) of the Gaussian function.

$$\mathrm{FWHM} = 2\sqrt{2\ln 2}\sigma. \quad (3)$$

The time resolution of the measurement system used in this work was estimated from the PALS spectra for iron plates ($10 \times 10 \times 0.3$ mm^3) which were heat-treated at 1273 K for 3 h in vacuum to decrease the concentration of lattice defects. The obtained spectra were analyzed using a fitting program for the time resolution, ResolutionFit in the PALSfit [75]. The obtained time resolutions were estimated to be 255(1) ps to 268(1) ps, which are comparable to the values obtained with other PALS measurement systems (200-300 ps). The cause of the distribution of the time resolutions is possibly an aging degradation of the photomultiplier tubes installed in the detectors.

In order to take into account the annihilation component in the Kapton films used for the ^{22}Na source, the positron lifetimes and intensities for the Kapton films were obtained from the PALS spectra for the above iron plates. One of the obtained spectra is shown in Fig. 13. The data was successfully reproduced by assuming three components. The lifetime and intensity for Component 1 were 109(1) ps and 86(1)%, respectively. Taking these values into consideration, this component was assigned to the positron annihilation events in the iron plates. The lifetime was consistent with that in α-Fe (111 ps) reported in a previous work [76]. The lifetime for Component 2 ranged from 376(5) ps to 386(4) ps, suggesting the positron annihilation events in the Kapton films because the values are consistent with that observed in the Kapton (385(1) ps) in Ref. [77]. The annihilation intensity in the Kapton film with a thickness of 7.5 μm was calculated to be 7% by a theoretical calculation for the positron annihilation ratio as a function of the sample thickness; however, the value obtained by the analysis was 15(1)%,

which is larger than the theoretical value [78]. The reason for the difference in the intensities may be due to the back scattering of positrons at the surface of the iron plates. Component 3 shows the positron lifetime with a few nanoseconds, which could be assigned to the annihilation events of Ps formed on the surface of the iron plates or in the glue on the Kapton tapes.

For the ZnO samples discussed in the subsequent chapters, the PALS spectra were obtained with sufficient statistics of 2×10^6 counts in total typically for one data and were also analyzed by assuming three components. The first component was assigned to the positron annihilation events in the bulk and/or at monovacancies such as isolated V_{Zn} and V_{Zn} complexes with impurities in the samples. The second component was assigned to the positron annihilation events in the Kapton films. For the analysis, the lifetime value for this component was fixed to that of Component 2 obtained for the iron standard sample each time right before the ZnO sample measurement. The third component was assigned to the annihilation events of Ps formed on the surface of the samples or in the glue on the Kapton films. Only the parameters for the first component reflecting the states of isolated V_{Zn} and V_{Zn} interacting with impurity elements are discussed in this paper.

2.4 Electric conductivity measurements

In order to identify the lattice defects contributing to the *n*-type conduction of the hydrothermally grown ZnO single crystals, in this work, electric conductivity measurements were performed. In this subsection, the experimental setup, the measurement method, and the data analysis are described.

2.4.1 Experimental setup

The electric property of the ZnO samples were characterized with the two-wire method using 2400 SourceMeter (Keithley). As shown in Fig. 14, conductive silver paste was applied on the samples in two rows and was thoroughly dried. After that, copper wires as the electrodes were contacted on the silver paste rows and were coated with the silver paste. The distance between the electrodes was about 5 mm. The applied voltage was controlled with a software Lab Tracer (Keithley), which can monitor the measurement current and time. The sample temperatures during the measurements were recorded with a type K thermocouple connected to midi LOGGER GL220 (Graphtec).

2.4.2 Measurement methods and data analysis

In the present work, the electric conductivity σ (S cm^{-1}) in the samples was evaluated by the following equation.

$$\sigma = \frac{I}{V} \times \frac{l}{S}. \tag{4}$$

Here, V, I, S, and, l indicate the voltage applied to the samples (V), the recorded current values (A), the cross section of the samples (cm^2), and the distance between the electrodes (cm), respectively.

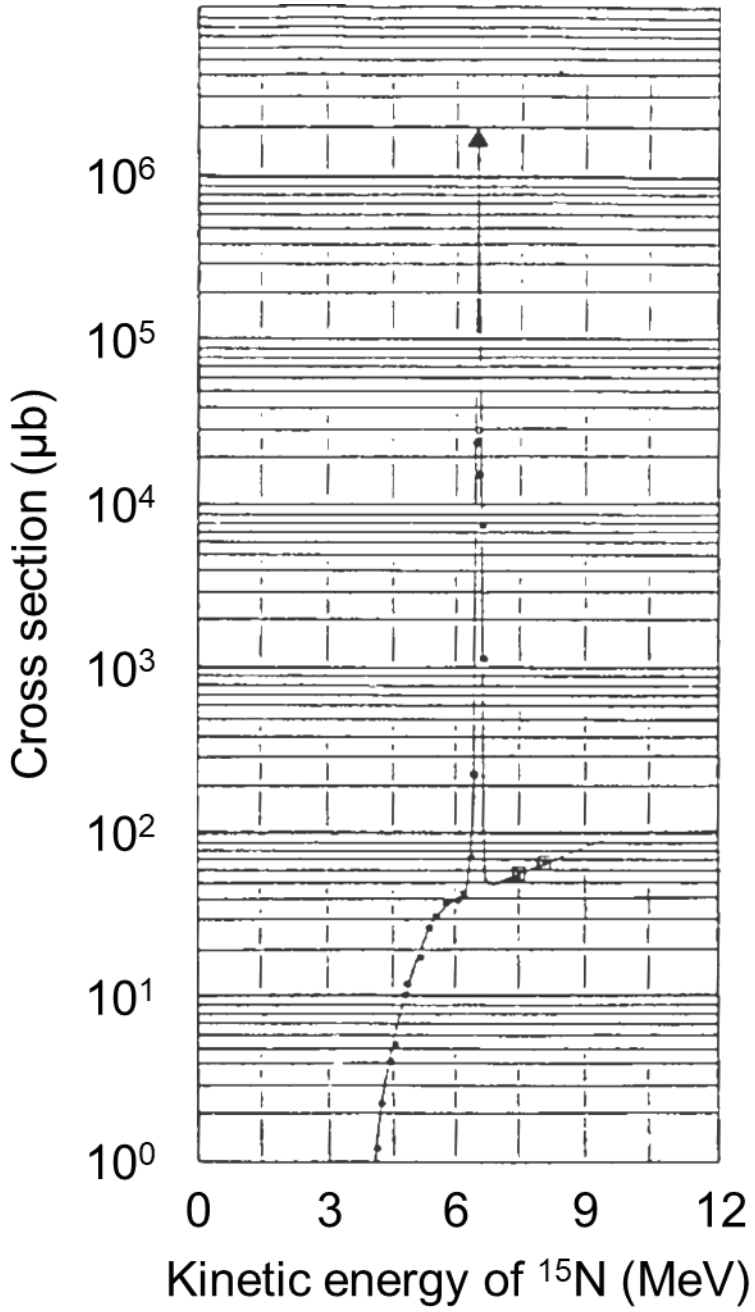

Fig. 6 The cross section of the nuclear reaction between ^{1}H and ^{15}N as a function of the kinetic energy of ^{15}N [68].

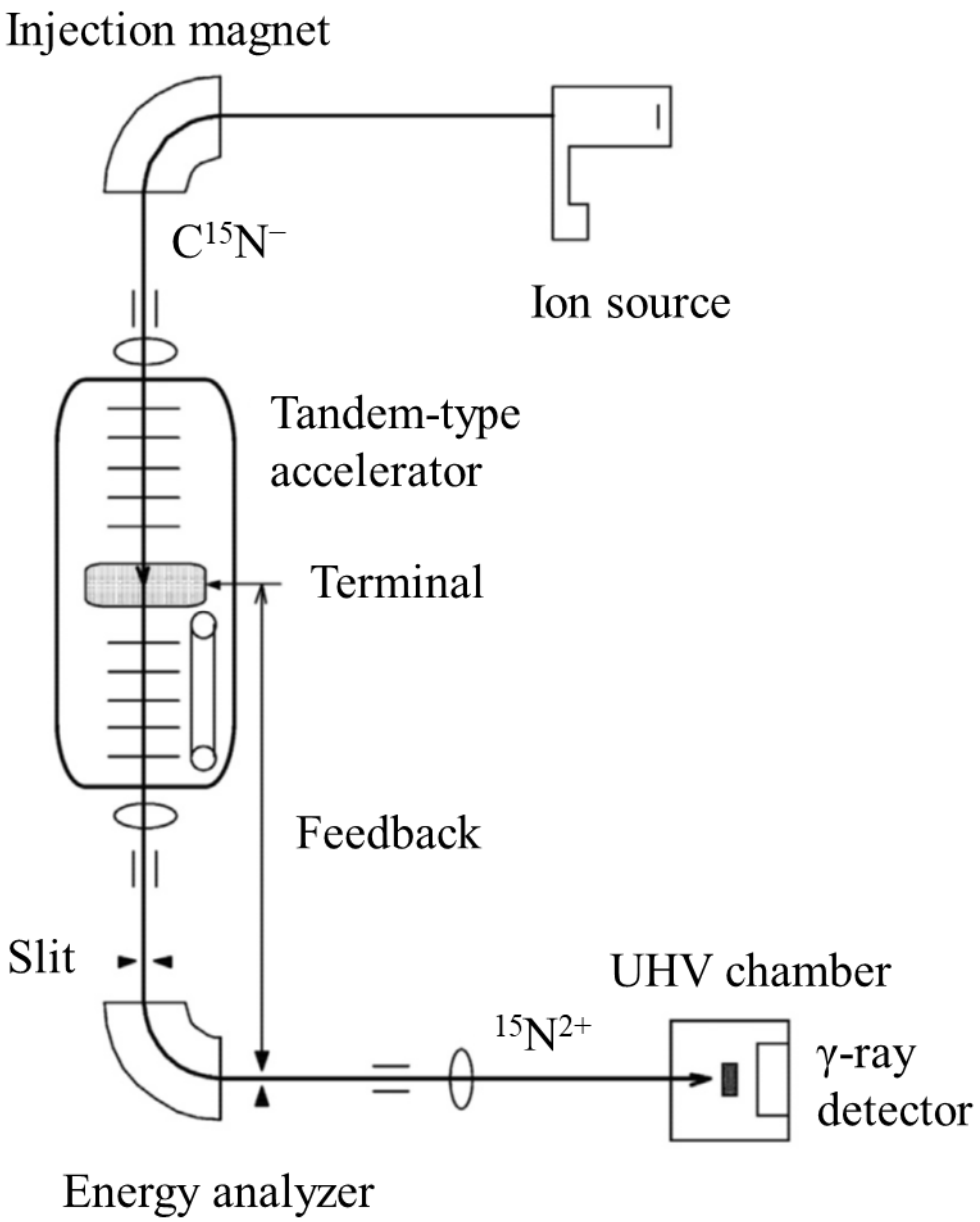

Fig. 7 Scheme of the tandem accelerator system for $^{1}H(^{15}N,\alpha\gamma)^{12}C$ NRA constructed in the MALT tandem accelerator facility of The University of Tokyo [68].

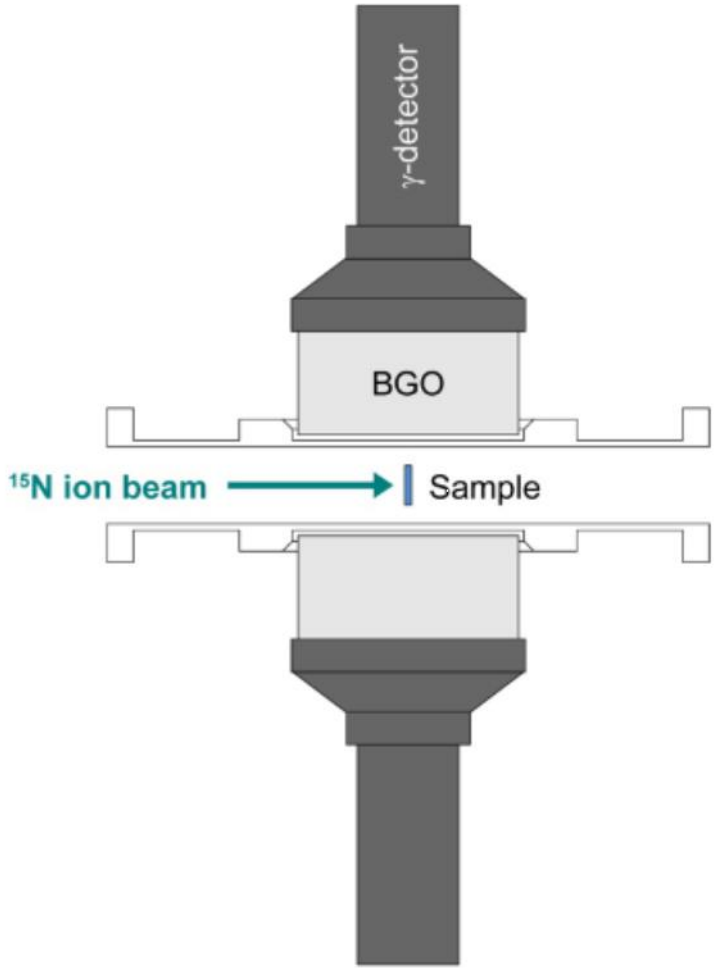

Fig. 8 Arrangement of the detectors for NRA installed at BL-2C beam line in the MALT tandem accelerator facility of The University of Tokyo [69].

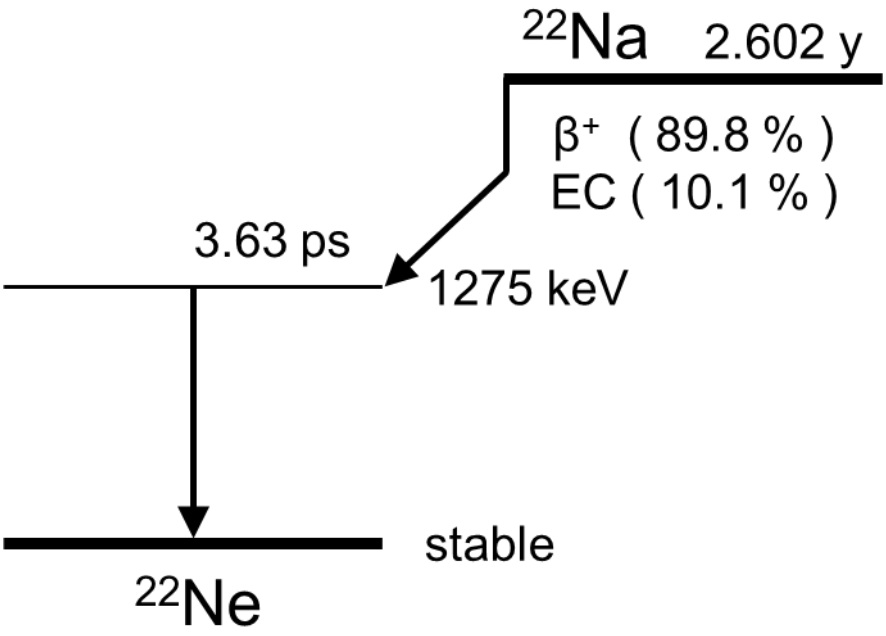

Fig. 9 Decay scheme of ^{22}Na [73].

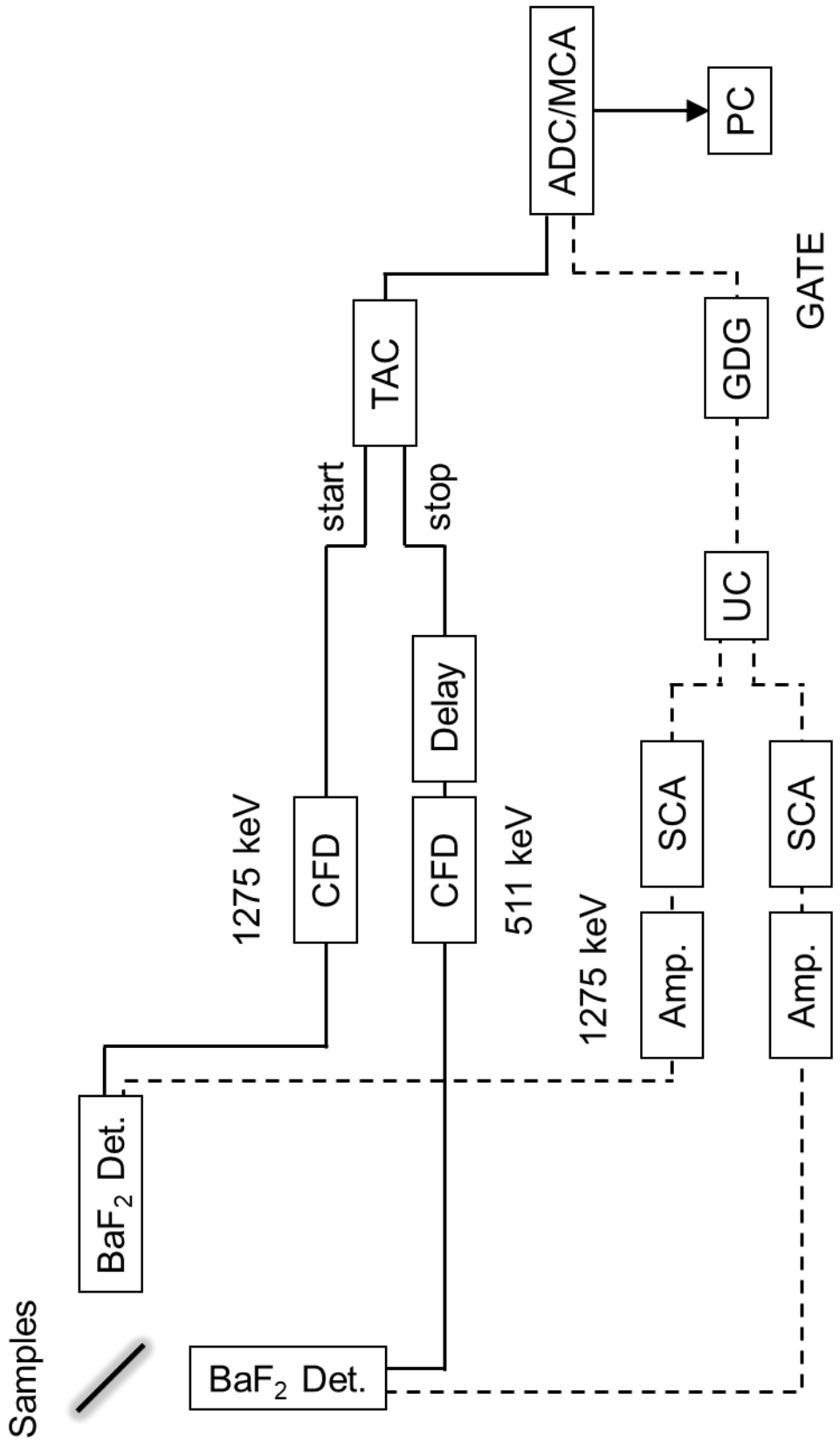

Fig. 10 Electric circuit for the present PALS measurement.

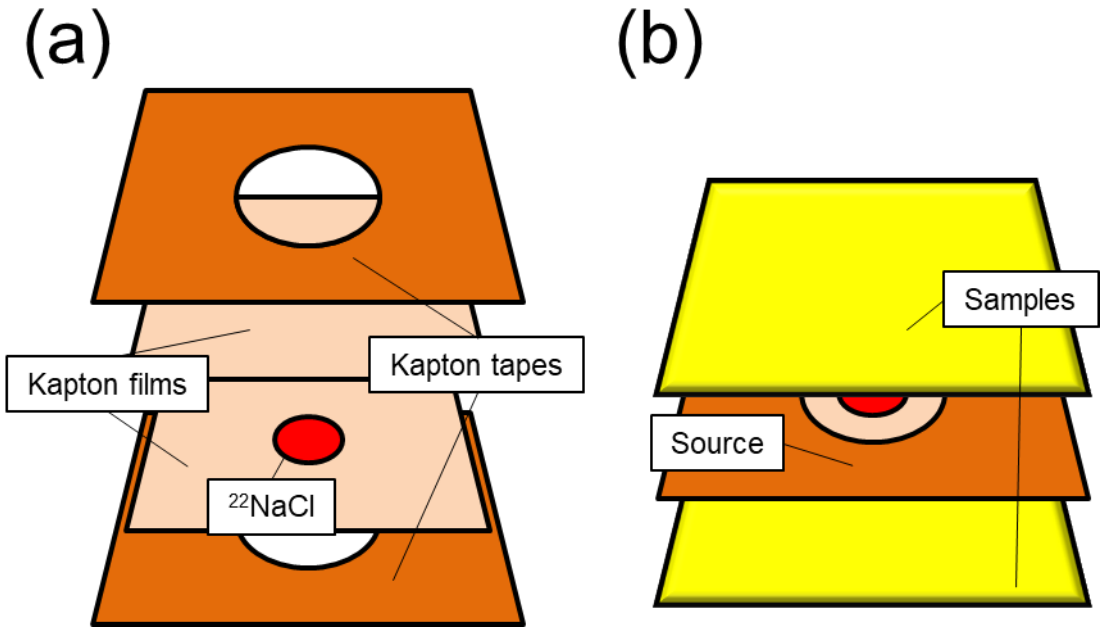

Fig. 11 (a) Composition of positron source of ^{22}Na and (b) the source sandwiched between samples.

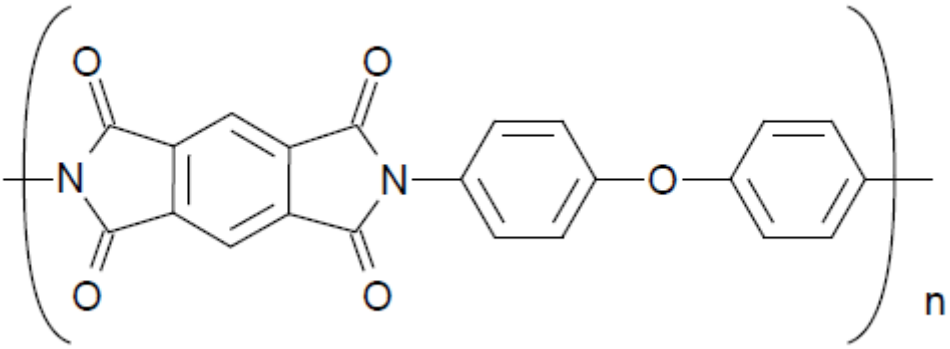

Fig. 12 Molecular structure of Kapton.

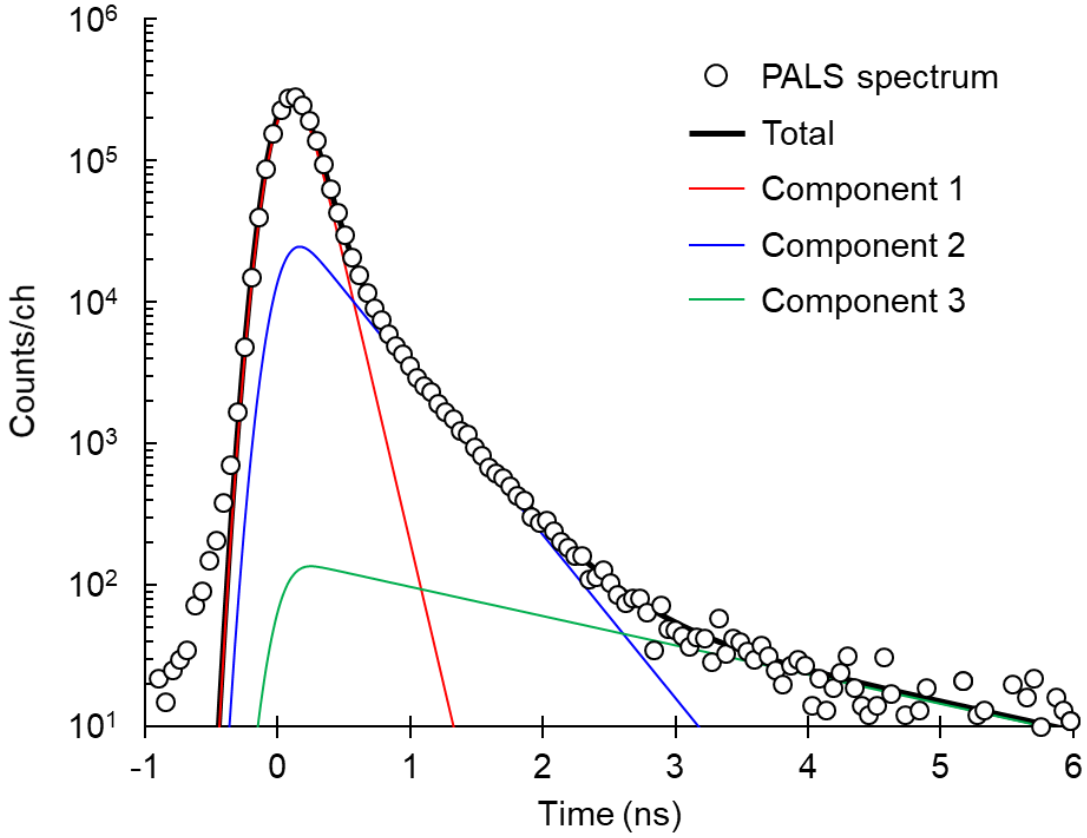

Fig. 13 PALS spectrum obtained for iron plates.

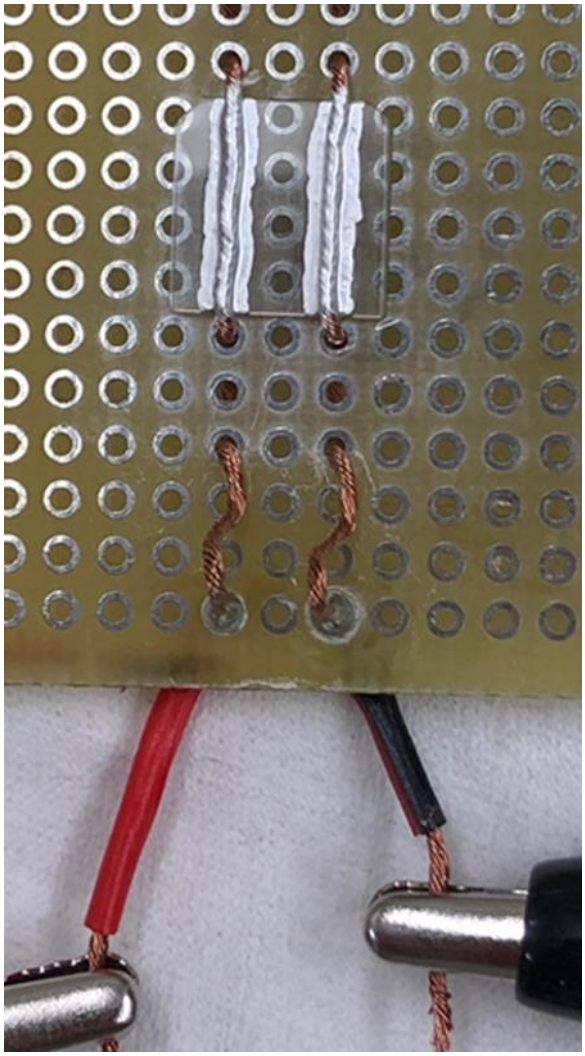

Fig. 14 Arrangement of the present electric conductivity measurement system.

Chapter 3 Impurity hydrogen atoms as donors contributing to *n*-type conduction of zinc oxide

3.1 Introduction

Recent progress in crystal growth techniques is remarkable, and high-quality crystals grown by hydrothermal growth methods are available. Growth rate by this method is slower by 2 orders of magnitude or more than that by the melting growth method, whereas it is possible to mass-produce single crystals by means of the hydrothermal growth method using large autoclaves, which is important for the production of ZnO-based electric devices. However, large amounts of hydrogen atoms (H) are likely to be involved in the crystal because water (H_2O) is used as the solvent in the method. H in the forms of H_i and H_O are considered to be the origins of the *n*-type conduction in undoped ZnO as described in Chapter 1. It is also known that H exist in ZnO as in [zinc vacancy]-hydrogen complexes (V_{Zn} + H) as depicted in Fig. 15 [79-81]. The presence of V_{Zn} + H in the hydrothermally grown ZnO single crystals was also confirmed in the author's previous work [82]. It is theoretically suggested that V_{Zn} + H behave as acceptors in ZnO [83]. Thus, it is important to determinate the H concentration and to investigate their thermal behaviors because the coexistence of these H should influence the conduction of ZnO. Unfortunately, there are few reports about the characterization of H in ZnO due to the lack of appropriate analytical methods for dilute H in solids.

One of the objectives of the present work is to determine the absolute concentration of H and to investigate their thermal behaviors in ZnO. In the present work, heat-treatment temperature dependence of the H concentration in the hydrothermally grown ZnO single crystals was examined by NRA experiments. In addition, the thermal stability of V_{Zn} + H was investigated by means of PALS. In order

to discuss the relation between the H concentration and the *n*-type conduction, electric conductivity measurements were performed for the above samples. In this chapter, different bound states of H involved in the ZnO lattice and their thermal stabilities are discussed, and their effect on the *n*-type conduction is evaluated.

3.2 Experiments

Firstly, composition and physical properties of as-grown ZnO single crystals were investigated by means of NRA, PALS, and electric conductivity measurements. (See Chapter 2 for general explanation of the experimental methods.) For the investigation of the thermal behavior of impurity H, each of the samples underwent step-by-step 1-h isochronal heat treatment at 393, 473, 573, 673, 773, 873, and 973 K in air, followed by rapid cooling to room temperature and subsequent characterization by the above methods at room temperature. The experimental procedure is shown in Fig. 16.

In the present NRA experiments, the single crystal ZnO samples shown in Fig. 2 were cut into pieces with a size of 5 × 5 × 0.5 mm^3 and were attached on a sample holder using a carbon tape as shown in Fig. 17. A glass plate and a Kapton film were also attached on the top and bottom of the sample holder as a beam monitor and a standard sample with a known concentration of ^1H, respectively. In the present work, the samples were irradiated with a 6.530-MeV $^{15}N^{2+}$ beam at surface-normal incidence in an irradiated area of ~4 mm^2. The site of the resonant nuclear reaction in the sample was estimated to be in a depth of ~56 nm from the surface based on the stopping power of ZnO (S_{ZnO} = 2.56 keV nm^{-1}), according to the calculation with the SRIM code [84]. Batch measurements for the 4.43-MeV γ rays were performed every 20 seconds. In the measurements, a beam current was confirmed to be ~30 nA using a Faraday cup during an interval time of 5 seconds between each batch measurement. In order to determine

the ^{1}H concentration in the ZnO samples, firstly, the γ-ray detection efficiency α in the measurement system was estimated from the NRA data for the Kapton film using the following equation.

$$\alpha = \frac{I \times S_{\mathrm{Kapton}}}{c_{\mathrm{H}}}. \tag{5}$$

Here, I indicates the γ-ray yield as net γ-ray counts normalized by the current of incident $^{15}N^{2+}$ ions, S_{Kapton} denotes the stopping power of the Kapton film (1.2879 keV nm^{-1}) [69], and c_{H} is the concentration of hydrogen atoms in the Kapton film (2.28×10^{22} cm^{-3}) [69], respectively. Substituting these values in Eq. (5), the present γ-ray detection efficiency was estimated to be $\alpha = 1.41(10) \times 10^{-19}$ counts μC^{-1} keV nm^{-1} cm^{3}. Using this α value and the stopping power of ZnO samples S_{ZnO}, the absolute concentration of ^{1}H in the ZnO samples was estimated from Eq. (5).

3.3 Results and discussion

3.3.1 Determination of the concentration of impurity hydrogen atoms in hydrothermally grown single crystal ZnO

In the present NRA experiments, the H concentration in the samples was obtained by batch measurements. For each sample annealed at different temperatures, the $^{15}N^{2+}$ dose dependence of the H concentration was obtained. Figure 18 shows the $^{15}N^{2+}$ dose dependence of the H concentration in the as-grown ZnO single crystal. The H concentration decreases asymptotically down to a constant value as the $^{15}N^{2+}$ dose increases. This tendency was also observed in a previous work, where the decreasing trend was ascribed to thermal diffusion of H [27]. The data was successfully fitted with

multiexponential decay functions assuming three components in this case: two decaying components (green and blue dashed lines) and a constant component (a red dashed line).

These components can be discussed based on thermal behaviors of H as depicted in Fig. 19. When a sample is irradiated with heavy ions, the incident ions transfer their kinetic energy to the lattice of the matrix through the interaction with atoms in the matrix. It is considered that local temperature rises up to 10^5-10^6 K by the energy transfer and local annealing is consequently caused [85]. In this work as well, it is inferred that H bound loosely to the ZnO lattice (hereafter denominated loosely bound hydrogens, LBH) would thermally diffuse out of the nuclear reaction site by the heat of the local annealing by the $^{15}N^{2+}$ beam; as a result, the H concentration decreases as the $^{15}N^{2+}$ dose increases. The different decay rates for the observed components reflect different diffusivities of LBH in the ZnO lattice; thus, LBH are classified into two groups LBH1 and LBH2, showing fast and slow diffusion, respectively. On the other hand, strongly bound H (SBH hereafter) hardly show thermal diffusion in the reaction site, and thus, a constant concentration of H was observed regardless of the $^{15}N^{2+}$ dose. Accordingly, the analysis result suggests that H take at least three different bound states in the as-grown ZnO samples. From the intersections of each fitting line and the ordinate of the graph in Fig. 18, the concentrations of LBH1, LBH2, and SBH in the as-grown sample were estimated to be 2.35(3), 0.59(2), and 0.22(1) at.%, respectively; these are overwhelming values compared with those of other impurity elements existing in the sample, suggesting that H would influence the bulk physical property of the ZnO sample.

Heat-treatment temperature dependence of the concentrations of each H in the hydrothermally grown ZnO single crystals is shown in Fig. 20. Each data was obtained by the same way as the case for the as-grown sample (Fig. 18). LBH1 was observed only in the as-grown sample but not in the heat-treated samples. This observation suggests that LBH1 diffuse out easily by heat treatment at 393 K, which can be understood

as meaning that the binding energy of LBH1 and the ZnO lattice is very low. The physical state of LBH1 will be discussed together with the results of electric conductivity measurements in Subsection 3.3.3.

The LBH2 were observed in the samples heat-treated at temperatures up to 673 K but disappeared above the temperature, which suggests that LBH2 are removed by heat treatment at the high temperature. The phenomenon can be seen from the $^{15}N^{2+}$ dose dependence for the samples heat-treated at different temperatures shown in Fig. 21. The concentration of LBH2 up to 673 K was almost unchanged though statistics of the data is not enough due to dilute concentration of H. Heat-treatment temperature dependence of the concentrations of H_i and H_O in ZnO obtained by a theoretical calculation is shown in Fig. 22 [38]. Here, the H_O concentration remains up to 673 K but decreases drastically at temperature range between 673 and 773 K. It is interesting that the thermal behavior of LBH2 obtained in the present work is analogous to the result of this calculation.

It was found that almost all SBH survived even at 973 K, which suggests that the thermal stability of SBH is considerably high. The average concentration of SBH in the temperature range of 393-973 K was estimated to be 0.10(3) at.%. The present result for the thermal stability of SBH is consistent with a previous theoretical calculation and experimental result for that of V_{Zn} + H [79,80]. Taking the present result and the reports into consideration, SBH possibly exist as V_{Zn} + H in ZnO. Thus, the thermal behavior of V_{Zn} + H was investigated by means of PALS to verify the above inference.

3.3.2 Thermal stability of V_{Zn} + H complex

Heat-treatment temperature dependence of positron lifetimes observed for the hydrothermally grown ZnO single crystals is shown in Fig. 23. The theoretical lifetimes of positrons annihilating in V_{Zn} (207 ps), in V_{Zn} + H (177-179 ps), and in bulk (154 ps) in ZnO are also indicated in the figure [27]. The positron lifetime observed in the as-grown

samples was 181(1) ps, demonstrating that almost all positrons annihilate in V_{Zn} + H according to the theoretical calculation. In addition, the positron lifetime remained unchanged even though the heat-treatment temperature rose up to 973 K. From the present PALS results, it is suggested that V_{Zn} + H are not thermally decomposed to V_{Zn} and H even at 973 K.

Figure 24 shows a theoretically deduced dependence of average positron lifetimes in monovacancies with different charge states in semiconductors on the concentrations of the vacancies [86]. τ_b and τ_d represent positron lifetimes in the bulk and in vacancies, respectively, which means that positron lifetimes become longer from τ_b to τ_d with increasing concentration of the vacancies. Almost all positrons annihilate in the vacancies with the charge states of 0, −1, and −2 at their concentrations above approximately 0.03 at.%, showing the positron lifetimes of τ_d. It is theoretically suggested that V_{Zn} + H in *n*-type ZnO take mainly the charge state of −1 [83]. Because it was found that almost all positrons annihilate in V_{Zn} + H complexes, it can be said that the concentration of V_{Zn} + H in the hydrothermally grown ZnO single crystals used in this work is above ~0.03 at.%. The observed concentration of SBH 0.10(3) at.% evidently suggests that SBH exist in the form of V_{Zn} + H.

3.3.3 Relation between impurity hydrogen atoms and *n*-type conduction

Heat-treatment temperature dependence of electric conductivity of the hydrothermally grown ZnO single crystals is shown in Fig. 25. The electric conductivity in the as-grown sample was 5.3(1) × 10^{-6} S cm^{-1}. For the heat-treated samples, the electric conductivity increased after heat treatment at 393 K. From the NRA result for the sample heat-treated at 393 K, it was found that highly concentrated LBH1 are removed out of the samples, which may have relation to the enhancement of the conductivity. H_2O molecules possibly involved in the lattice would scatter the

conduction electrons as large lattice defects. Thus, removal of the interstitial H_2O enables higher electric conduction. This inference is supported by a report that H_2O adsorbing to the ZnO surface are removed out by a heat treatment at ~370 K [87].

Decreasing electric conductivity with increasing temperature from 473 K to 973 K was observed. In previous works, it was found that the electron mobilities in the ZnO samples heat-treated at 673-973 K are unchanged [88,89]. These observations allow ones to infer that the decrease in the electric conductivity observed in the present samples mainly arises from decrease in the carrier concentration. However, the observed electric conductivity is correlated simply neither with the concentration of LBH2 nor with that of SBH in the temperature range between 473 and 973 K. In general, the carrier concentration in the system is the difference between the concentrations of donors and acceptors. Here, the decreasing tendency of the conductivity is discussed assuming that LBH2 and SBH play roles of the donors as H_O and acceptors as V_{Zn} + H, respectively. Taking into account the constant concentration of LBH2 in the temperature range between 473 K to 673 K, the decreasing tendency of the electric conductivity could be attributed to the activation of the acceptor property of V_{Zn} + H existing in the samples. The activation of the acceptors means that their holes become mobile. According to a previous work, oxygen molecules are adsorbed on the surface of ZnO samples under oxygen atmosphere in the temperature range of 373-623 K [90]. If V_O exist in the present samples and cancel out V_{Zn} + H, it is considered that V_O incorporate with the oxygen molecules by heat-treatment in air, resulting in the activation of the acceptor property of V_{Zn} + H, which leads to deactivation of the donor property of LBH2. In addition, a previous work reports that the H concentration decreases step-by-step in the temperature range of 773-973 K [63], which suggests that the decreasing tendency of the electric conductivity above 673 K may arise from decrease in the concentration of LBH2. Another cause of the decreasing conductivity may be the decrease of LBH2 existing near

the sample surface. For the corroboration of the above conjecture, it is necessary to investigate the thermal behavior of H existing near the surface by means of NRA using ^{15}N ions with low incident energy.

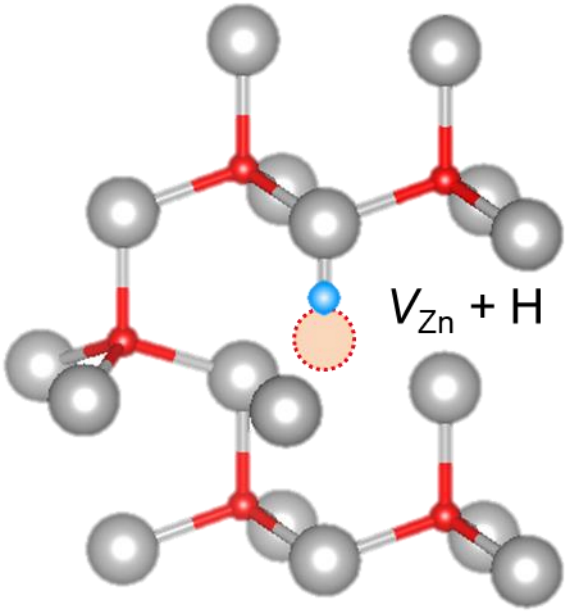

Fig. 15 Schematic illustration of (zinc vacancy)-hydrogen complex in ZnO.

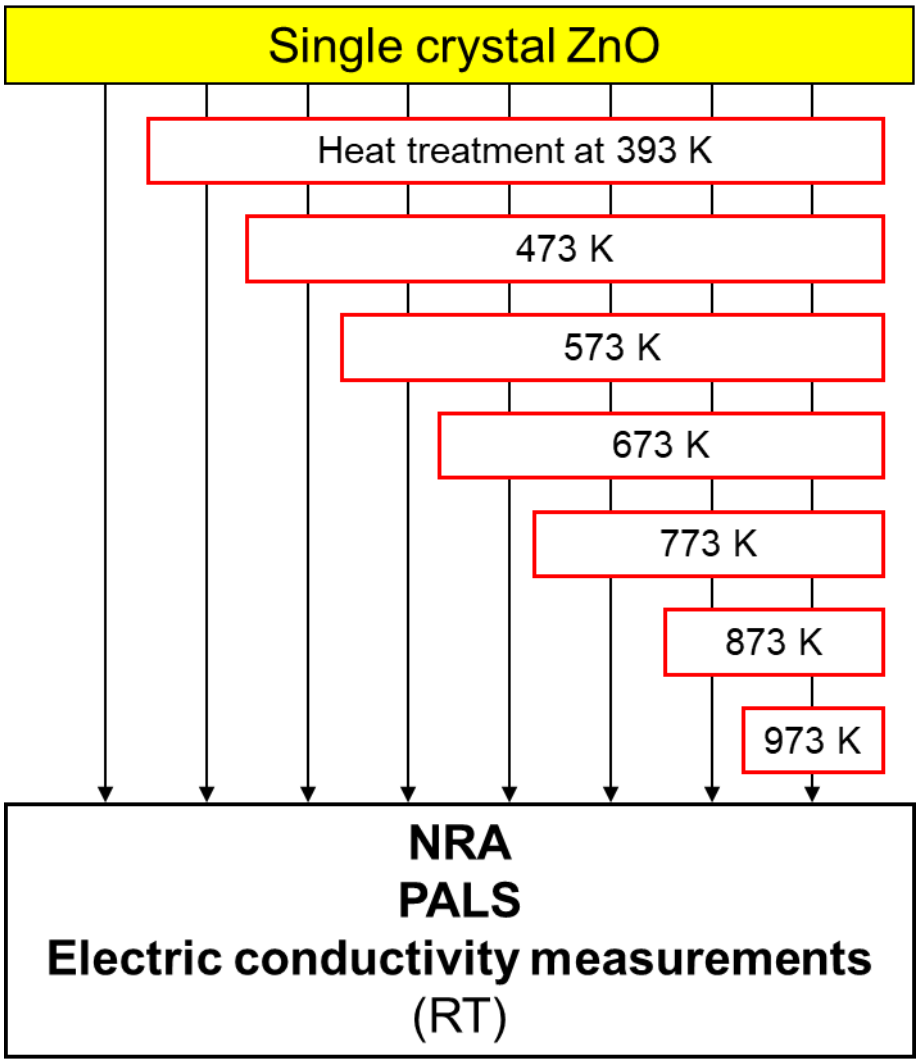

Fig. 16 Experimental procedure. The samples were heat-treated at the indicated temperature in air for 1 h in advance, and NRA, PALS, and electric conductivity measurements were performed.

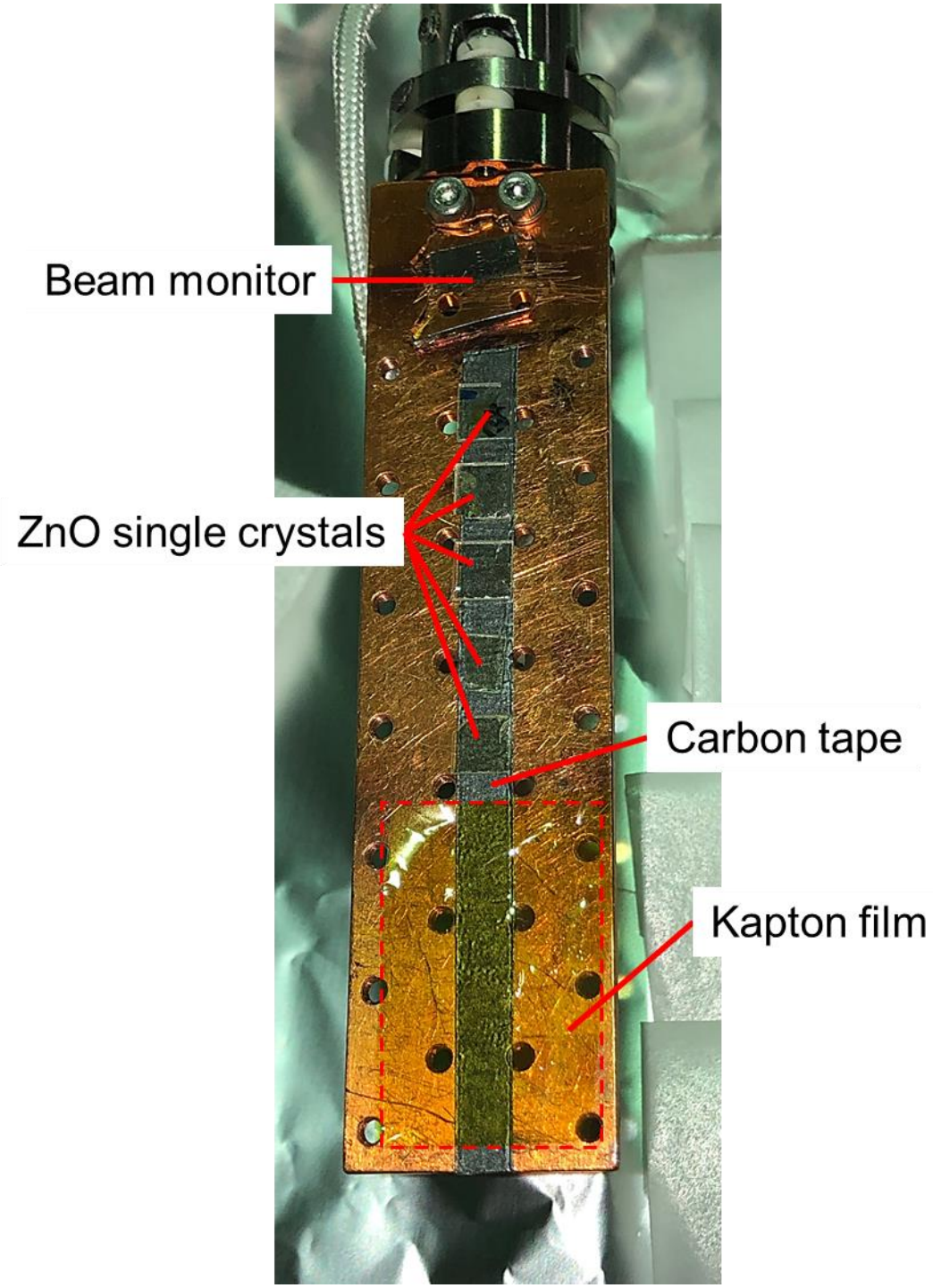

Fig. 17 Sample holder for NRA and the arrangement of measurement samples. The Kapton film is attached in the red dashed area.

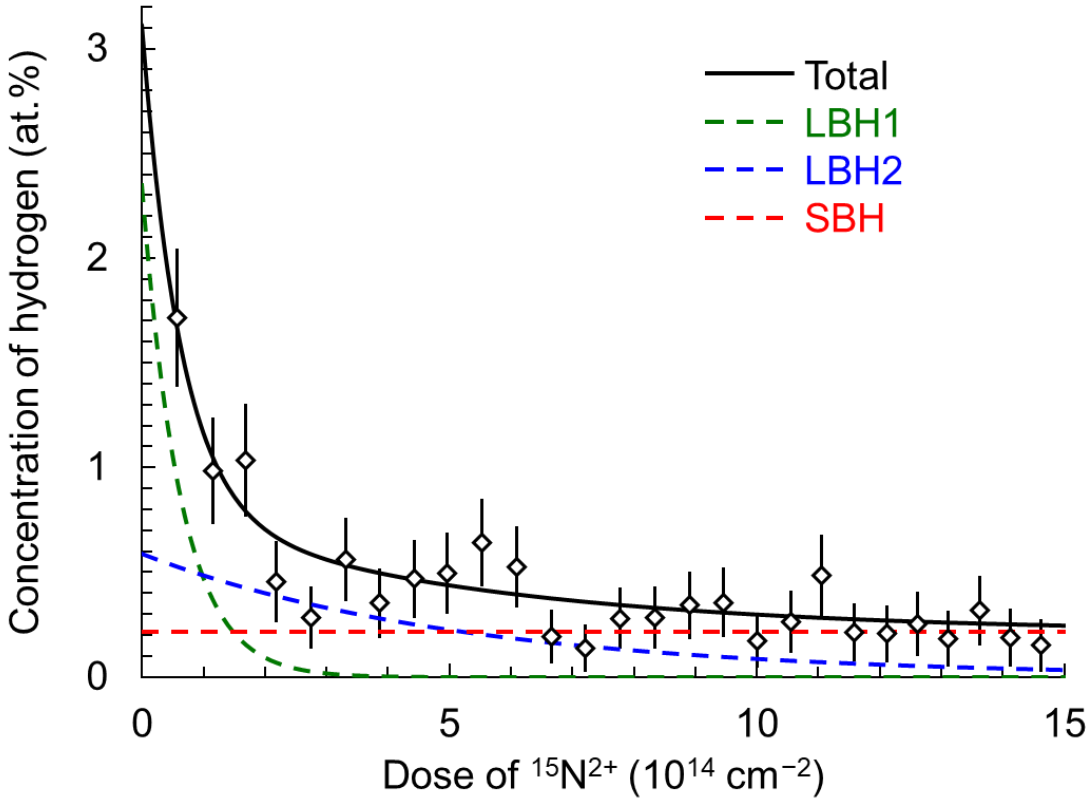

Fig. 18 $^{15}N^{2+}$ dose dependence of the H concentration in an as-grown ZnO single crystal. The components LBH1, LBH2, and SBH are indicated by green, blue, and red dashed lines, respectively.

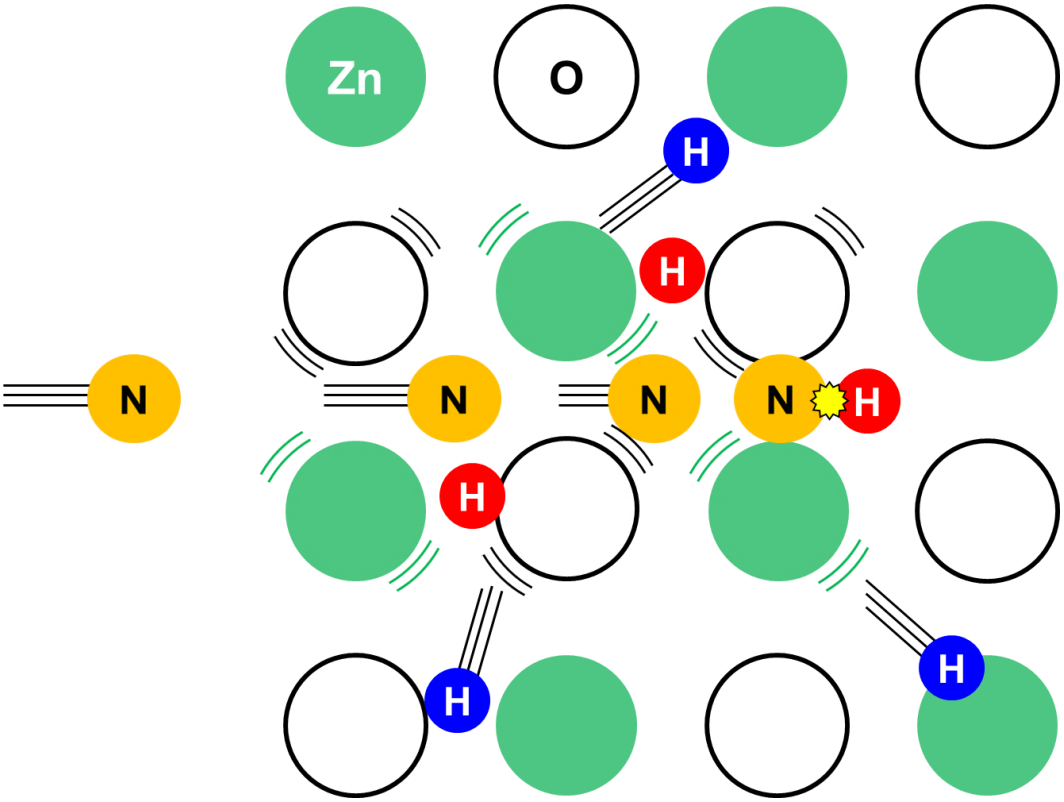

Fig. 19 Schematic illustration of thermal diffusion of impurity hydrogen atoms caused by energetic $^{15}N^{2+}$ ions.

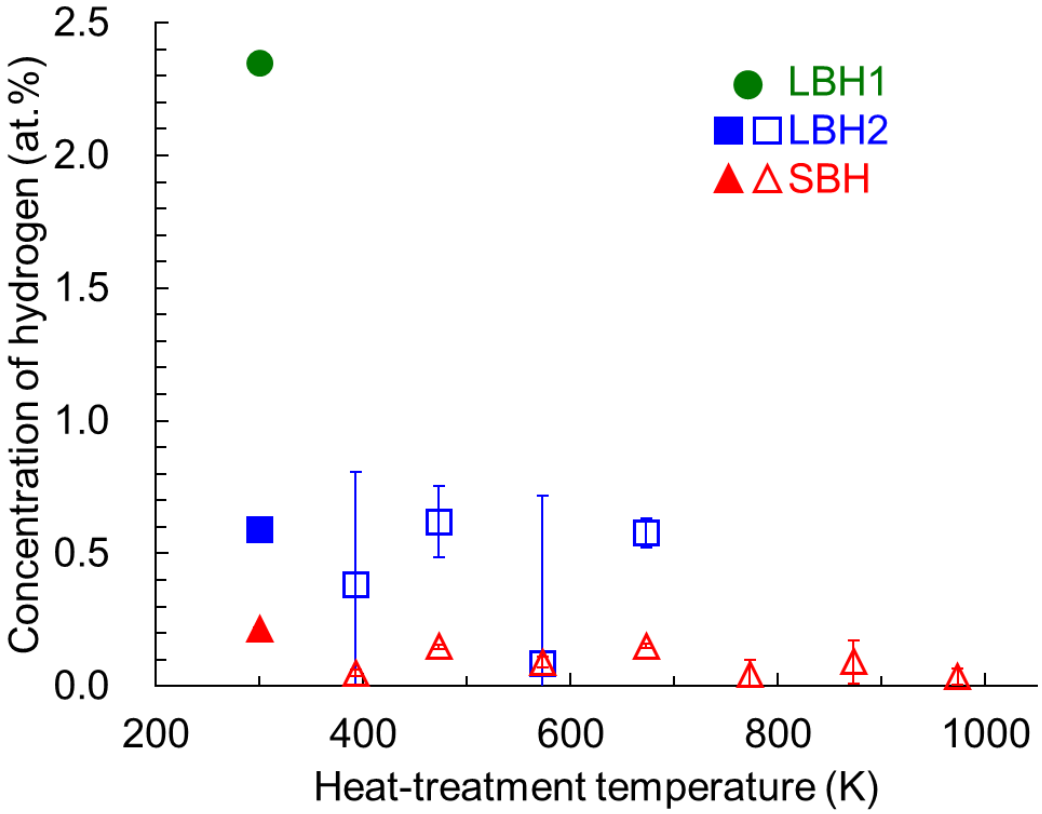

Fig. 20 Heat-treatment temperature dependence of the concentration of impurity hydrogen atoms. The solid symbols represent the data for the as-grown sample.

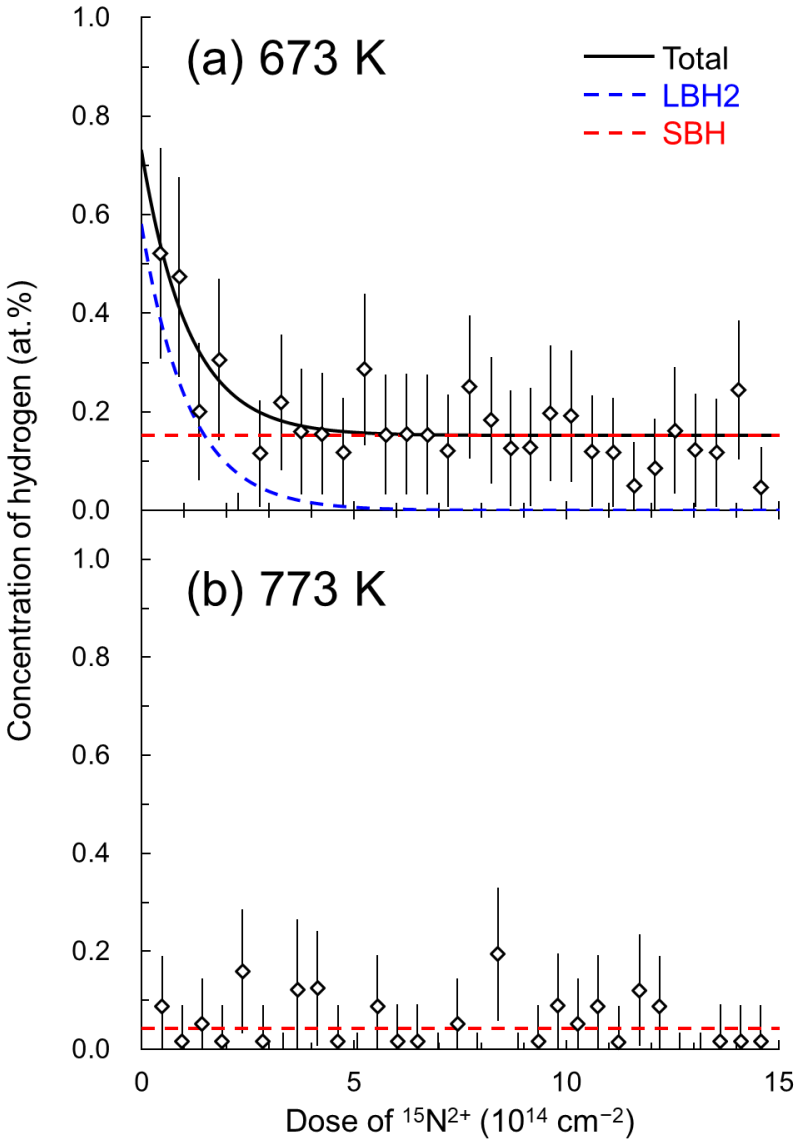

Fig. 21 $^{15}N^{2+}$ dose dependence of the H concentration in the ZnO single crystals heat-treated (a) at 673 K and (b) at 773 K. The components LBH2 and SBH are indicated by blue and red dashed lines, respectively. As for Fig. 21(b), only a red dashed line is depicted for simplicity.

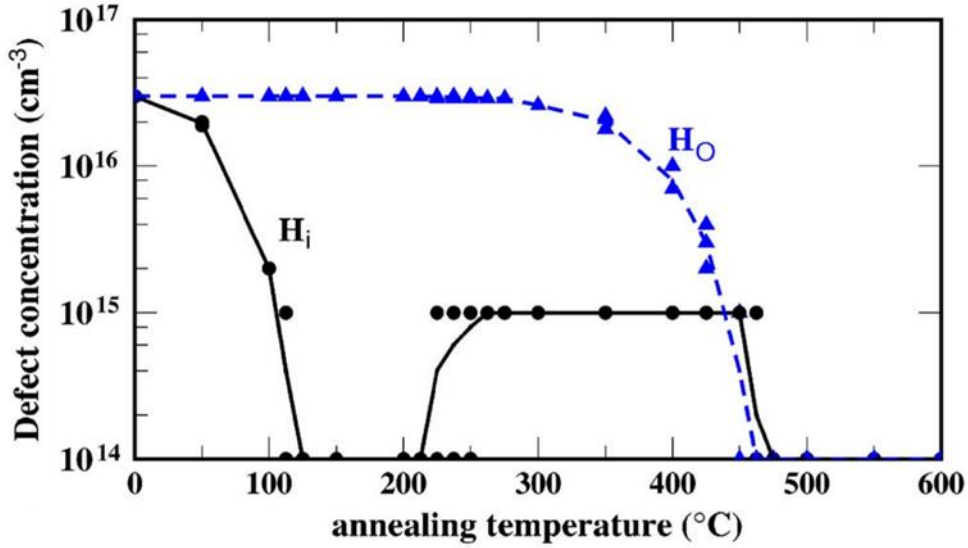

Fig. 22 Heat-treatment temperature dependence of the concentration of H_i and H_O in ZnO obtained with kinetic Monte Carlo simulations [38].

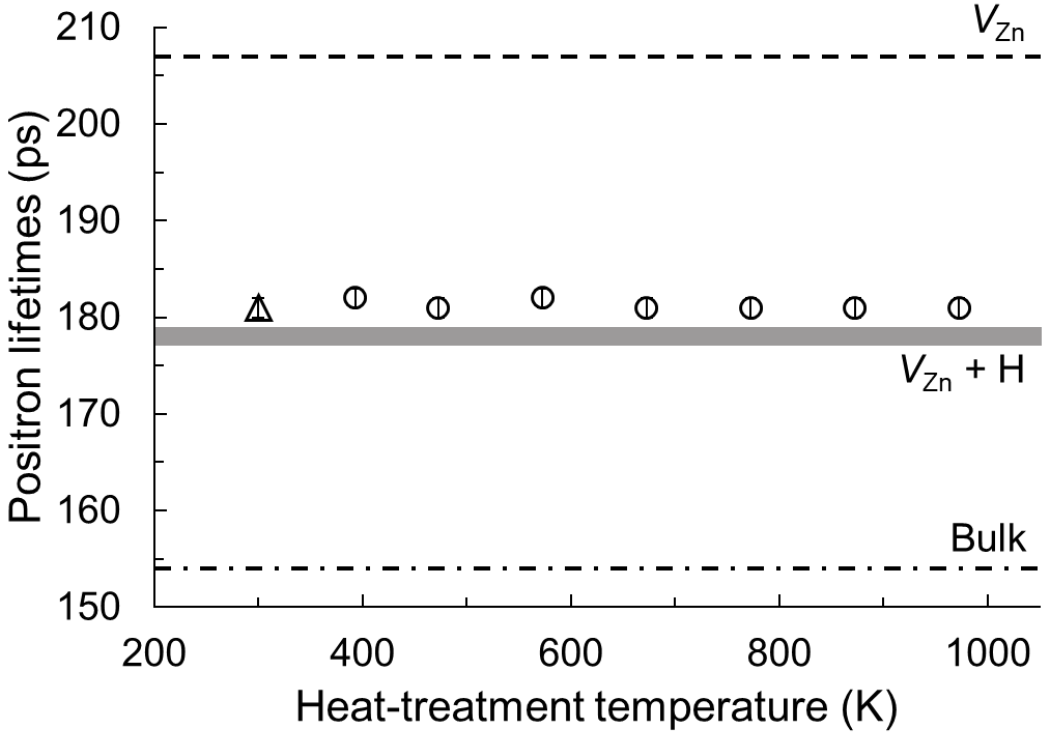

Fig. 23 Heat-treatment temperature dependence of the positron lifetimes in ZnO. The triangle symbol represents the data for the as-grown sample. The theoretical lifetimes of positrons annihilating in V_{Zn} (207 ps), in V_{Zn} + H (177-179 ps), and in the bulk (154 ps) are also indicated [27].

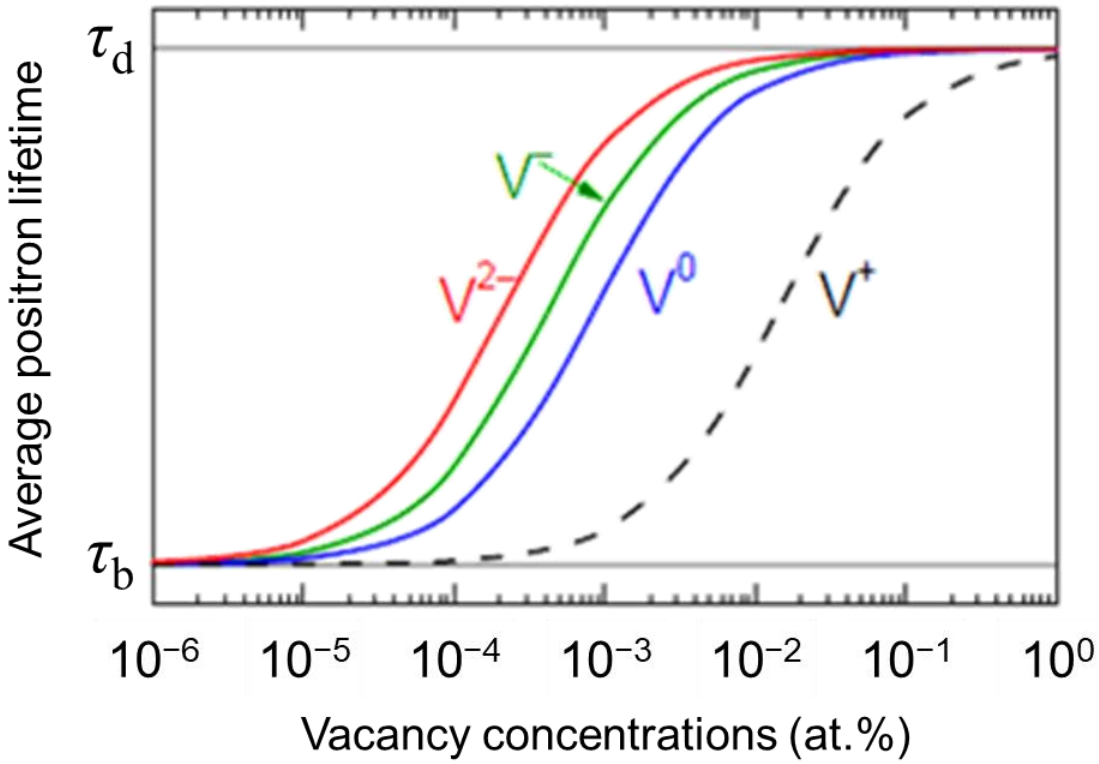

Fig. 24 Average positron lifetimes calculated as a function of concentration of monovacancies of different charge states in semiconductors [86].

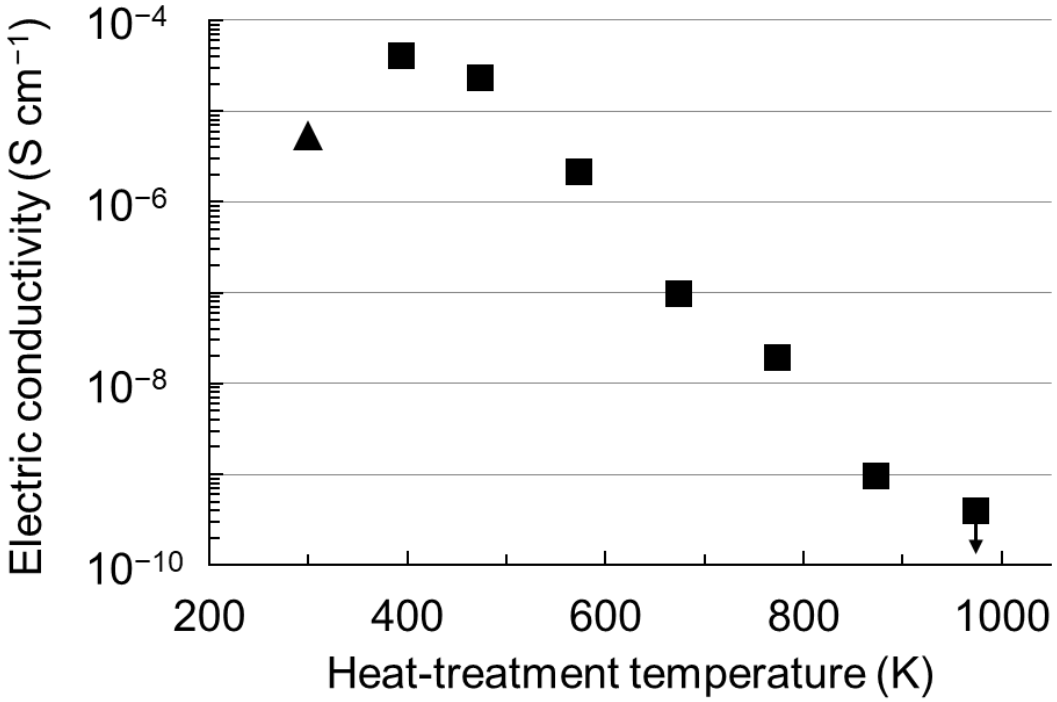

Fig. 25 Heat-treatment temperature dependence of the electric conductivity in the ZnO samples. The triangle symbol represents the data for the as-grown sample. The upper limit is shown for the electric conductivity at 973 K.

Chapter 4 Interactions of intrinsic lattice defects formed by heat treatments and their contribution to electric conductivity

4.1 Introduction

In the previous chapter, it was demonstrated that the electric conductivity of the hydrothermally grown ZnO single crystals decreases markedly with increasing temperature up to 973 K. On the other hand, increase of the electric conductivity of the ZnO sample was observed above the temperature in some previous works, which suggests that the origin is the formation of intrinsic lattice defects in ZnO such as Zn_i and V_O by heat treatments at high temperature because ZnO is free of H at this high temperature [16,17]; however, the mechanism of the generation of carriers has not been revealed. As was described in Chapter 1, when Zn_i are originated from Zn_{Zn}, V_{Zn} are also formed simultaneously as a Frenkel defect; therefore, detailed carrier cancellation mechanism between them should be investigated.

The objective of the present work is to reveal the mechanism of the generation of the carriers originated from the above intrinsic defects. In order to evaluate their contribution to the electric conductivity, electric conductivity measurements and PALS were employed. Here, a new mechanism of the intrinsic-defect induced *n*-type conduction is proposed.

4.2 Experiments

4.2.1 Heat-treatment temperature dependence

In accordance with the experimental procedure shown in Fig. 26(a), the hydrothermally grown ZnO single crystals underwent step-by-step 1-h isochronal heat

treatment at 973, 1073, 1173, 1273, 1373, and 1473 K in air, followed by rapid cooling to room temperature for the investigation of the formation and thermal behavior of the intrinsic defects. After each heat treatment, time variation of electric conductivity under light irradiation and sample warming were observed at room temperature.

4.2.2 Heat-treatment time and atmosphere dependences

In order to investigate the influence of the formation of V_O on the electric conduction, the samples were heat treated at 1473 K for 1 or 12 h in air or in an oxygen gas flow, followed by rapid cooling to room temperature. The experimental procedure is shown in Fig. 26(b). After the heat treatments under each condition, electric conductivity measurements and PALS were performed at room temperature.

4.2.3 Time variation of electric conductivity under light irradiation and sample warming

The author tried to identify the defects formed during the heat treatments by means of electric conductivity measurements during time-varying electron excitation-deexcitation process by light-irradiation and warming. The ZnO samples were exposed to a visible light with a photon energy of about 2.7 eV from an InGaN lamp for the first 1800 seconds to make electrons on defect levels of deep donors photo-excited, and for the subsequent 1800 seconds, the samples were screened from the light to let the electrons in the conduction band deexcited. However, temperature of the samples was inevitably raised by radiant heat from the lamp during the light irradiation and electrons on defect levels of shallow donors in the samples were likely to undergo thermal excitation. In order to evaluate the effect and degree of the thermal excitation, conductivity measurements were performed in the dark while temperature of the samples was raised using a heater up to the same temperature as that recorded under the light irradiation. Figure 27 shows expected conduction-variation patterns for the results obtained by both

methods. The ordinates and abscissas are the electric conductivity and elapsed time in the excitation and deexcitation processes, respectively. The black and red lines represent the conductivity variation for the case of light-irradiation and warming, respectively. “ON” and “OFF” denote the start and stop times of the excitation, respectively. For the termination of the excitation, the samples are screened from the light or heat. The following four kinds of the results are expected.

(1) If the concentration of the defects is, if any, lower than the detection limit of the conductivity measurements, the electric conductivity remains zero under both excitation processes. (Fig. 27(a))

(2) When only deep donors exist in the sample, increase-decrease tendency of the electric conductivity is observed only in the measurement under the photoexcitation. (Fig. 27(b))

(3) When only shallow donors exist in the sample, increase-decrease tendency of the electric conductivity is observed in both measurements. (Fig. 27(c)) The illustration corresponds to the case that the sample is warmed to the same temperature by both excitation methods.

(4) When deep and shallow donors coexist in the sample, the increase-decrease tendency is observed in both measurements, but maximum value of the electric conductivity during the light-irradiation is larger than that during the warming even though the sample temperatures in both measurements are the same because of additional contribution by the photoexcitation. (Fig. 27(d))

In the case of the patterns (3) and (4), the electric conductivity possibly exceeds zero because electrons of the shallow donors are excited to the conduction band even by the thermal energy of room temperature. The above simulation would help the author to infer whether there exist deep and/or shallow donors in the sample. In the sections below, the obtained results are discussed in three heat-treatment temperature ranges: 973

K, 1073-1273 K, and 1373 K. Hereafter, the sample heat-treated at 973 K, for example, is denominated S973 for simplicity.

4.3 Results and discussion

4.3.1 Heat-treatment temperature dependence of electric conductivity of ZnO single crystals

Heat-treatment temperature dependence of the electric conductivity of the hydrothermally grown ZnO single crystals is shown in Fig. 28. The electric conductivity increases drastically in contrast to the results shown in Fig. 25. It is considered that the cause of increase in the electric conductivity is the formation of the intrinsic defects during the heat treatments because H as extrinsic shallow donors are removed out of the samples in this temperature range [63].

4.3.2 Contribution to electric conduction of intrinsic defects formed by heat treatments

4.3.2.1 *Formation of intrinsic lattice defects during heat treatments*

The electric conductivities as a function of elapsed time during the excitation by the light-irradiation and warming for S973, S1073, S1173, and S1273 are shown in Figs. 29(a)-29(d), respectively. As shown in Fig. 29(a), an increase-decrease tendency was not observed in the measurement for S973, which suggests that lattice defects contributing to the electric conduction were hardly formed by the heat treatment at 973 K.

For S1073, S1173, and S1273 shown in Figs. 29(b)-29(d), respectively, two remarkable changes were observed. One is the baseline of the electric conductivity exceeding zero, which signifies the presence of shallow donors. More specifically, the conductivity increased stepwisely with increasing heat-treatment temperature, which is

apparently seen in the higher baseline for S1273 than that for S1073. The candidate of the shallow donors is limited to Zn_i because H are diffused out of the sample by heat treatments at these temperature range [63]. The other change is the observation of excess increase in the electric conductivity by the light-irradiation. This observation indicates that V_O as deep donors were formed by the heat treatment at 1073 K and higher. A previous work reported that some oxygen atoms are annealed out of the ZnO sample by heat treatment at temperature above 1023 K, suggesting the formation of V_O [91]. In some previous photoluminescence studies, it is found that the intensity of photo-emission peak at ~2.5 eV increases drastically at temperature above 1073 K, which indicates that the defect level of V_O at 2.5 eV below the conduction band of ZnO were generated [23,25,92,93]; it should be noted that the present results are consistent with those of the reports above. The results obtained in this work suggest that Zn_i and V_O coexist in the sample heat-treated at temperature between 1073 K and 1273 K and contribute to the conduction as the shallow and deep donors, respectively (see Fig. 27(d)).

4.3.2.2 *Contribution of interstitial zinc atoms and oxygen vacancies to electric conduction*

Figure 30 shows the electric conductivities and sample temperatures as functions of elapsed time during the excitation by both methods for S1373. It is interesting that the results for S1373 are different from those for S1273. As shown in Fig. 30, in both measurements, it is found that time variation of the electric conductivities is similar to that of the sample temperatures. If both of the photoexcitation and thermal excitation take place, the electric conductivity should be larger by the former excitation than the latter as observed for S1273. The fact that the maximum values in both measurements are almost the same for S1373 suggests that only Zn_i contribute to the conduction but V_O do not (see Fig. 27(c)). Namely, the contribution of V_O to the *n*-type conduction seems

disappeared in the observation for S1373. Here, the origin of the inactivation of V_O is discussed. In general, Frenkel defect pairs of donors and acceptors such as Zn_i and V_{Zn} cannot contribute to the conduction because of charge cancellation between each other. However, assuming the coexistence of V_O with them, V_O can cancel out with V_{Zn}, resulting in survival of electrically active Zn_i; therefore, the present observation for S1373 can be interpreted as meaning that only Zn_i contribute to the conduction without charge cancellation with V_{Zn}. For V_O, they release their electrons to cancel out with V_{Zn} and thus become inactive even under the light irradiation.

4.3.3 Effect of formation of V_O on electric conduction

In order to verify the validity of the above inferred mechanism, conductivity measurements were performed for the samples heat-treated under different oxygen partial pressures and evaluated the effect of V_O on the electric conductivity. Heat-treatment time and atmosphere dependences of the electric conductivity in the hydrothermally grown ZnO single crystals are shown in Fig. 31. In the case of heat treatments in air, the electric conductivity improved as the treatment time increased. In addition, positron lifetimes remained almost unchanged even under the same treatment condition as shown in Table 2; therefore, it is considered that there is no additional formation of Zn_i and V_{Zn}. These results indicate that the charge cancellation of V_O and V_{Zn} proceeded due to increase in the V_O concentration by the high-temperature heat treatments in air.

On the other hand, the electric conductivity decreased after the heat treatment under an oxygen gas flow. This observation suggests that V_O incorporate with oxygen atoms and the V_O concentration decreases because of higher oxygen partial pressure compared with air. These results support the mechanism inferred above.

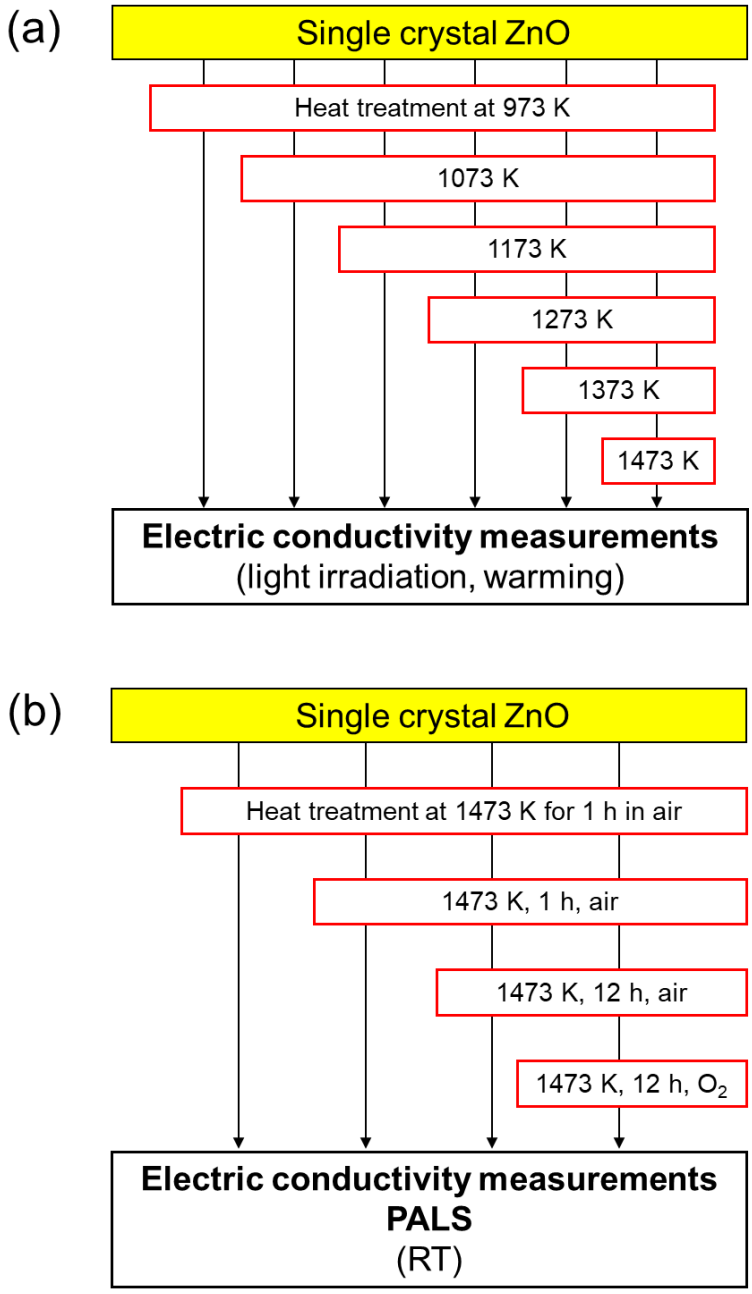

Fig. 26 Experimental procedures (a) for heat-treatment temperature dependence and (b) for heat-treatment time and atmosphere dependence. In the experimental procedure (a), the samples were heat-treated at indicated temperatures in air for 1 h.

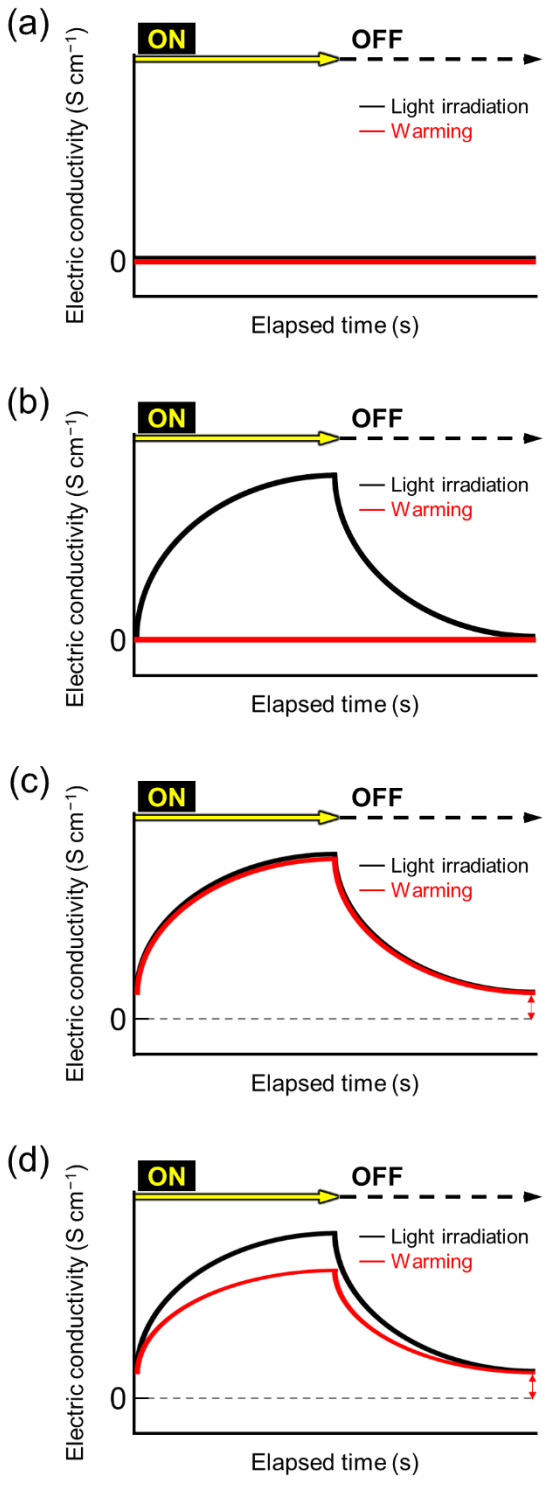

Fig. 27 Expected conduction-variation patterns as functions of the measurement time. See the text for the explanation.

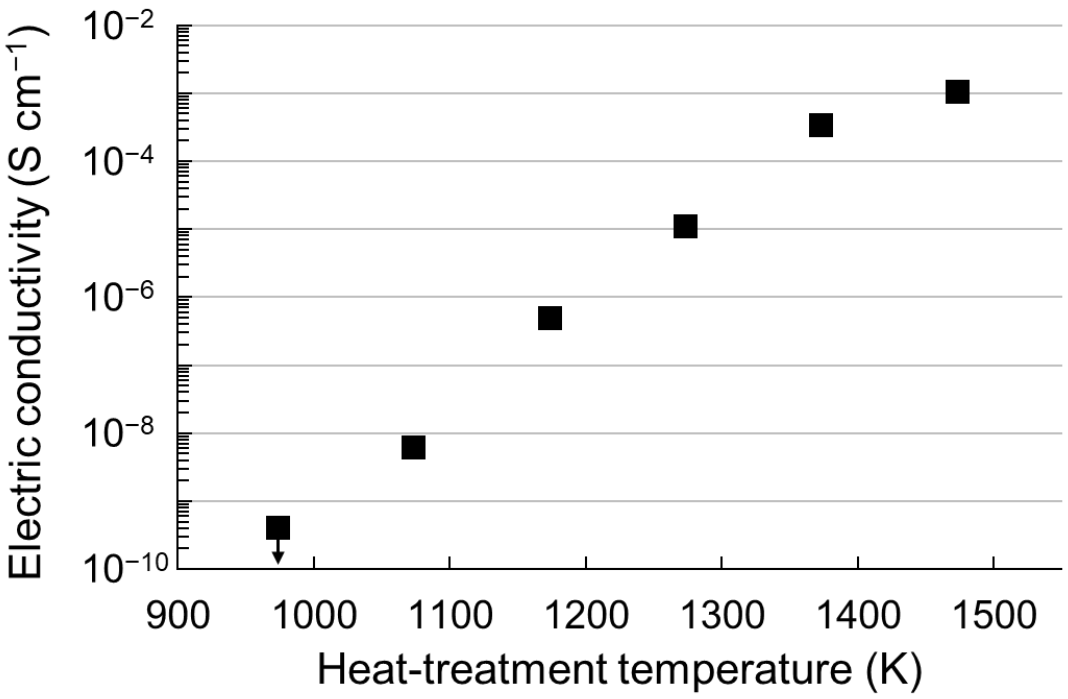

Fig. 28 Heat-treatment temperature dependence of the electric conductivity in the ZnO sample. The upper limit is shown for electric conductivity at 973 K.

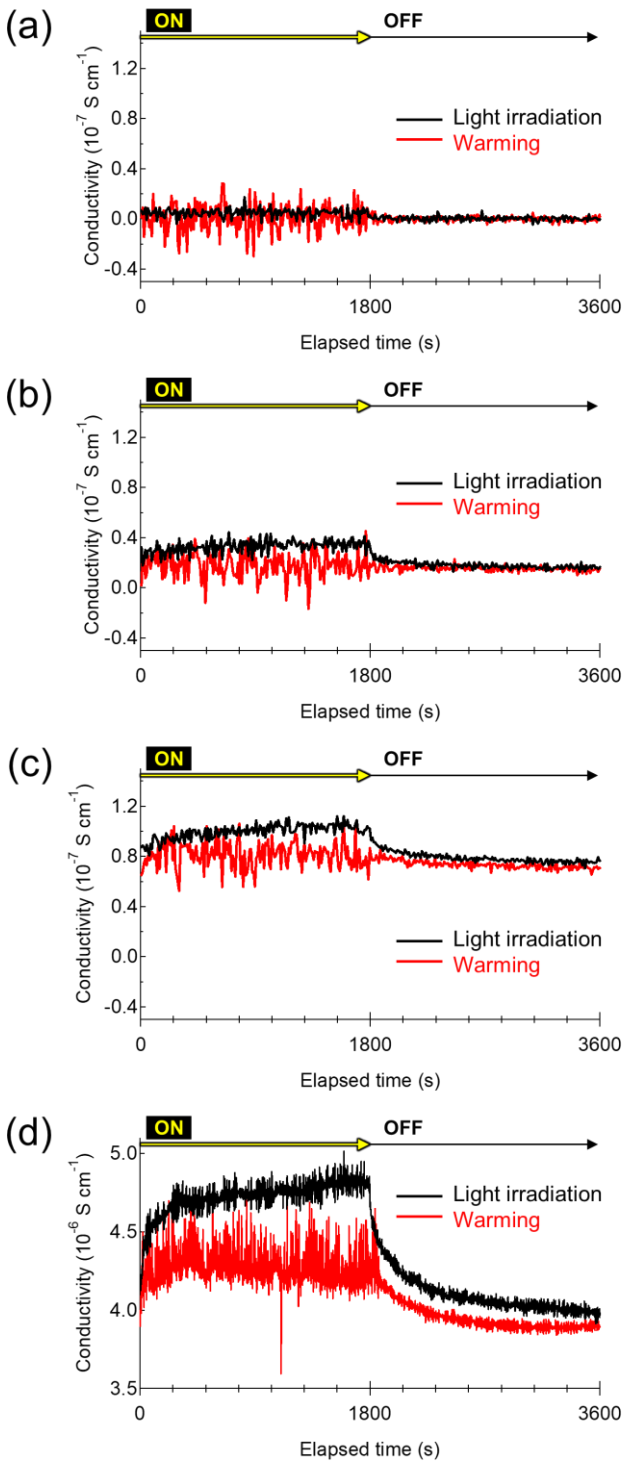

Fig. 29 Time variations of the conductivities as functions of elapsed time of light irradiation (black line) and of sample warming (red line) observed (a) for S973, (b) for S1073, (c) for S1173, and (d) for S1273.

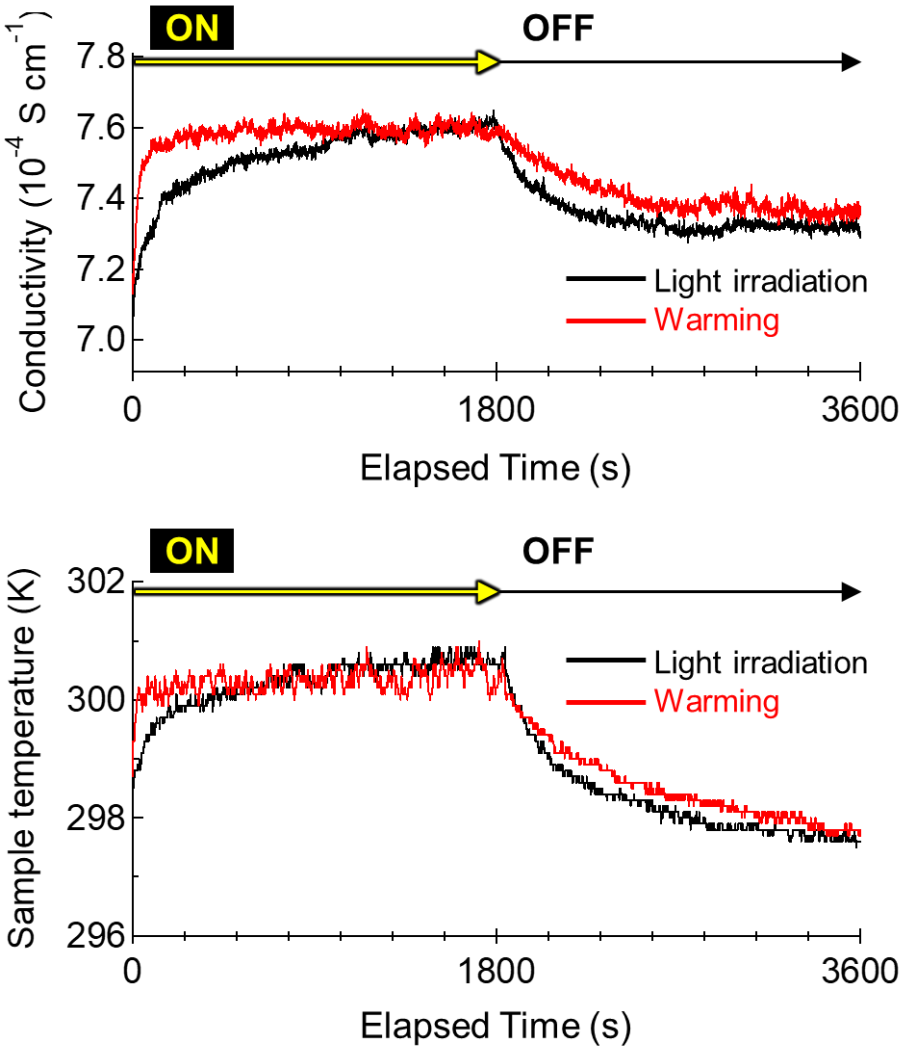

Fig. 30 Time variations of the conductivity and sample temperature for S1373 as functions of elapsed time of light irradiation (black line) and of sample warming (red line).

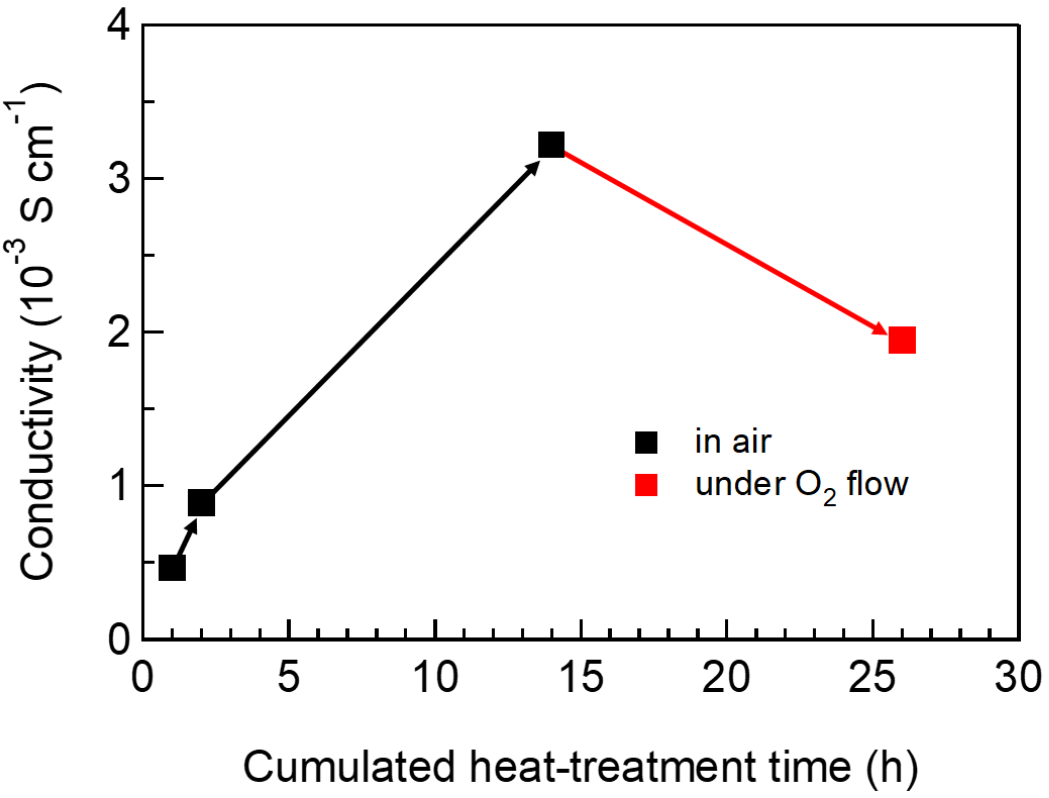

Fig. 31 Cumulated heat-treatment time and atmosphere dependences of the conductivity. The sample was heat treated at 1473 K in air and under O_2 gas flow as indicated by black and red arrows, respectively, and the conductivity measurements were performed at room temperature.

Table 2 Lifetimes of positrons annihilated in single crystal ZnO samples heated under respective conditions corresponding to those in Fig. 31. The value for the as-grown ZnO is listed together.

Heat-treatment condition			Positron lifetime (ps)
Temperature (K)	Heating time (h)	Atmosphere	
300 (as-grown)	—	—	181(1)
1473	1	Air	184(1)
1473	1	Air	185(1)
1473	12	Air	186(1)
1473	12	Oxygen gas flow	186(1)

Chapter 5 Summary

ZnO has received high expectation as an alternative material to replace semiconductors applied to functional devices such as transparent electrodes and light-emitting diodes. It is well known that even undoped ZnO shows the *n*-type conduction. The origin of the conduction is considered to be intrinsic lattice defects such as oxygen vacancies (V_O) and interstitial zinc atoms (Zn_i) formed by heat treatments and impurity hydrogen atoms (H) involved during the crystal growth; however, there is no unified view for the origin. In this work, $^{1}H(^{15}N,\alpha\gamma)^{12}C$ nuclear reaction analysis (NRA), positron annihilation lifetime spectrometry (PALS), and electric conductivity measurements were employed to detect the lattice defect species contributing to the *n*-type conduction. From the microscopic and macroscopic point of view, the states of being, thermal behaviors, and electric properties of the above lattice defects formed in hydrothermally grown ZnO single crystals were investigated. The results obtained in this work are summarized below.

5.1 Impurity hydrogen atoms contributing to *n*-type conduction of ZnO

Toward the elucidation of the origin of the *n*-type conduction, NRA, PALS, and electric conductivity measurements were performed for the ZnO samples heat-treated at different temperatures to investigate the concentration and thermal behavior of H as the primary candidate of the conduction.

The present NRA results for the as-grown sample indicated that there are two kinds of loosely bound H having different diffusivities (LBH1 and LBH2) and a strongly bound H (SBH). It was found that LBH1 are removed out of the sample at 393 K. The concentration of LBH2 remains almost unchanged up to 673 K but decreases abruptly

above the temperature. The thermal behavior of LBH2 is similar to a theoretical behavior of H substituting for lattice oxygen atoms. On the other hand, SBH survive at an average concentration of 0.10(3) at.% by the heat treatment even at 973 K. The present PALS study indicates that the thermal stability of [zinc vacancies]-H complexes (V_{Zn} + H) is considerably high and their concentration was estimated to be above 0.03 at.% in the samples by a comparative study with a previous theoretical calculation. From the information on their thermal stability and concentration, it is suggested that SBH exist as V_{Zn} + H. The conductivity of the ZnO sample increased at 393 K but decreased stepwisely in the temperature range of 473-973 K. Taking into consideration the present method adopted for the electric conductivity measurement, these results may reflect the states of H existing near the outermost surface. In order to evaluate the effect of surface H on the electric conductivity, it is necessary to investigate their thermal behavior on the outermost surface by means of NRA with a low-energy incident ^{15}N beam.

5.2 Intrinsic lattice defects contributing to *n*-type conduction of ZnO

The mechanism of the intrinsic-defect induced *n*-type conduction of undoped ZnO was investigated by means of electric conductivity measurements and PALS for the samples heat-treated at high temperature. For the heat treatment above 1073 K, the formation of deep and shallow donors was observed. They were identified as V_O and Zn_i from the results of the electric conductivity measurements through the observation of excitation-deexcitation behavior of carrier electrons by the light-irradiation and warming. Both of them contribute to the conduction of the sample heat-treated at temperature up to 1273 K. However, at 1373 K, the conductivity was enhanced only by thermal excitation, which suggests that only Zn_i contribute to the conduction but V_O do not.

From the electric conductivity measurements for the sample heat-treated in different oxygen partial pressures, it was found that the conductivity increases at lower oxygen partial pressure but decreases at higher pressure. These observed facts suggest that the formation of V_O cancels out the acceptor effect of V_{Zn}, leading to the activation of the donor effect of Zn_i.

References

[1] Z. Tan, W. Zhang, Z. Zhang, D. Qian, Y. Huang, J. Hou, Y. Li, Adv. Mater. **24**, 1476 (2012).

[2] P. T. Tue, S. Inoue, Y. Takamura, T. Shimoda, Appl. Phys. A **122**, 623 (2016).

[3] K. L. Chopra, S. Major, D. K. Pandya, Thin Solid Films **102**, 1 (1983).

[4] S. M. Mclennan, Geochem. Geophys. Geosystems **2**, 2000GC000109 (2001).

[5] T. Minami, Thin Solid Films **516**, 5822 (2008).

[6] T. Yamamoto, T. Yamada, A. Miyake, H. Makino, N. Yamamoto, J. SID **16**, 713 (2008).

[7] H. Liu, V. Avrutin, N. Izyumskaya, Ü. Özgür, H. Morkoç, Superlattices Microstruct. **48**, 458 (2010).

[8] Y. Liu, Y. Li, H. Zeng, J. Nanomater. **2013**, 1 (2013).

[9] A. Ziemińska-Stolarska, M. Barecka, I. Zbiciński, E3S Web Conf. **19**, 02026 (2017).

[10] C. W. Litton, D. C. Reynolds, T. C. Collins (Eds.), Zinc Oxide Materials for Electronic and Optoelectronic Device Applications, John Wiley and Sons, 2011.

[11] D. G. Thomas, J. Phys. Chem. Solids **3**, 229 (1957).

[12] S. J. Pearton, D. P. Norton, K. Ip, Y. W. Heo, T. Steiner, Prog. Mater. Sci. **50**, 293 (2005).

[13] H. Morkoç, Ü. Özgür, Zinc Oxide Fundamentals, Materials and Device Technology, Wiley-VCH, 2009.

[14] E. Ohshima, H. Ogino, I. Niikura, K. Maeda, M. Sato, M. Ito, T. Fukuda, J. Crystal Growth **260**, 166 (2004).

[15] Y. B. Zhang, G. K. L. Goh, K. F. Ooi, S. Tripathy, J. Appl. Phys. **108**, 083716 (2010).

[16] M. Jiang, D. D. Wang, B. Zou, Z. Q. Chen, A. Kawasuso, T. Sekiguchi, Phys. Stat. Sol. A **209**, 2196 (2012).

[17] W. Feng, S. Cho, M. Wang, D. D. Dung, Phys. Lett. A **380**, 480 (2016).

[18] J. Kaupužs, A. Medvids, P. Onufrijevs, H. Mimura, Opt. Laser Technol. **111**, 121 (2019).

[19] A. Janotti, C. G. Van de Walle, Phys. Rev. B **76**, 165202 (2007).

[20] L. Schmidt-Mende, J. L. MacManus-Driscoll, Mater. Today **10**, 40 (2007).

[21] A. A. Sokol, S. A. French, S. T. Bromley, C. R. A. Catlow, H. J. J. van Dam, P. Sherwood, Faraday Discuss. **134**, 267 (2007).

[22] F. Oba, A. Togo, I. Tanaka, J. Paier, G. Kresse, Phys. Rev. B **77**, 245202 (2008).

[23] L. C. Ann, S. Mahmud, S. K. M. Bakhori, Appl. Sur. Sci. **265**, 137 (2013).

[24] J. Čížek, J. Valenta, P. Hruška, O. Melikhova, I. Procházka, M. Novotný, J. Bulíř, Appl. Phys. Lett. **106**, 251902 (2015).

[25] M. A. K. Purbayanto, E. Nurfani, O. Chichvarina, J. Ding, A. Rusydi, Y. Darma, Appl. Sur. Sci. **462**, 466 (2018).

[26] D. C. Look, J. W. Hemsky, J. R. Sizelove, Phys. Rev. Lett. **82**, 2552 (1999).

[27] G. Brauer, W. Anwand, D. Grambole, J. Grenzer, W. Skorupa, J. Čížek, J. Kuriplach, I. Procházka, C. C. Ling, C. K. So, D. Schulz, D. Klimm, Phys. Rev. B **79**, 115212 (2009).

[28] S. F. J. Cox, E. A. Davis, S. P. Cottrell, P. J. C. King, J. S. Lord, J. M. Gil, H. V. Alberto, R. C. Vilão, J. P. Duarte, N. Ayres de Campos, A. Weidinger, R. L. Lichti, S. J. C. Irvine, Phys. Rev. Lett. **86**, 2601 (2001).

[29] K. Shimomura, K. Nishiyama, R. Kadono, Phys. Rev. Lett. **89**, 255505 (2002).

[30] C. G. Van de Walle, Phys. Rev. Lett. **85**, 1012 (2000).

[31] G. A. Shi, M. Stavola, S. J. Pearton, M. Thieme, E. V. Lavrov, J. Weber, Phys. Rev. B **72**, 195211 (2005).

[32] E. V. Lavrov, F. Herklotz, J. Weber, Phys. Rev. B **79**, 165210 (2009).

[33] F. Herklotz, E. V. Lavrov, J. Weber, Phys. B **404**, 4349 (2009).

[34] J. J. Dong, X. W. Zhang, J. B. You, P. F. Cai, Z. G. Yin, Q. An, X. B. Ma, P. Jin, Z. G. Wang, P. K. Chu, Appl. Mater. Interfaces **2**, 1780 (2010).

[35] J. K. Park, K. W. Lee, C. E. Lee, Appl. Phys. Lett. **103**, 023109 (2013).

[36] M. Wang, G. Yu, W. Ji, L. Li, W. Ding, L. Peng, Chem. Phys. Lett. **627**, 7 (2015).

[37] A. Janotti, C. G. Van de Walle, Nat. Mater. **6**, 44 (2007).

[38] J. Bang, K. J. Chang, Appl. Phys. Lett. **92**, 132109 (2008).

[39] K. S. Chan, L. Vines, K. M. Johansen, E. V. Monakhov, J. D. Ye, P. Parkinson, C. Jagadish, B. G. Svensson, J. Wong-Leung, J. Appl. Phys. **114**, 083111 (2013).

[40] X. Xue, T. Wang, X. Jiang, J. Jiang, C. Pan, Y. Wu, Cryst. Eng. Comm. **16**, 1207 (2014).

[41] H. Takenaka, D. J. Singh, Phys. Rev. B **75**, 241102(R) (2007).

[42] C. Soci, A. Zhang, B. Xiang, S. A. Dayeh, D. P. R. Aplin, J. Park, X. Y. Bao, Y. H. Lo, D.Wang, Nano Lett. **7**, 1003 (2007).

[43] H. K. Yadav, K. Sreenivas, V. Gupta, J. Appl. Phys. **107**, 044507 (2010).

[44] H. Endo, M. Sugibuchi, K. Takahashi, S. Goto, S. Sugimura, K. Hane, Y. Kashiwaba, Appl. Phys. Lett. **90**, 121906 (2007).

[45] D. Liu, T. L. Kelly, Nature Photon. **8**, 133 (2014).

[46] Y. I. Alivov, E. V. Kalinina, A. E. Cherenkov, D. C. Look, B. M. Ataev, A. K. Omaev, M. V. Chukichev, D. M. Bagnall, Appl. Phys. Lett. **83**, 4719 (2003).

[47] F. Gao, D. Zhang, J. Wang, H. Sun, Y. Yin, Y. Sheng, S. Yan, B. Yan, C. Sui, Y. Zheng, Y. Shi, J. Liu, Appl. Phys. Lett. **108**, 261103 (2016).

[48] A. Chen, H. Zhu, Y. Wu, M. Chen, Y. Zhu, X. Gui, Z. Tang, Adv. Funct. Mater. **26**, 3696 (2016).

[49] D. M. Hofmann, D. Pfisterer, J. Sann, B. K. Meyer, R. Tena-Zaera, V. Munoz-Sanjose, T. Frank, G. Pensl, Appl. Phys. A **88**, 147 (2007).

[50] H. Hirasawa, M. Yoshida, S. Nakamura, Y. Suzuki, S. Okada, K. Kondo, Sol. Energy Mater. Sol. Cells **67**, 231 (2001).

[51] M. N. Jung, J. E. Koo, S. J. Oh, B. W. Lee, W. J. Lee, S. H. Ha, Y. R. Cho, J. H. Chang, Appl. Phys. Lett. **94**, 041906 (2009).

[52] P. M. R. Kumar, C. S. Kartha, K. P. Vijayakumar, F. Singh, D. K. Avasthi, Mater. Sci. Eng. B **117**, 307 (2005).

[53] J. Rousset, E. Saucedo, D. Lincot, Chem. Mater. **21**, 534 (2009).

[54] J. G. Lu, Y. Z. Zhang, Z. Z. Ye, Y. J. Zeng, H. P. He, L. P. Zhu, J. Y. Huang, L. Wang, J. Yuan, B. H. Zhao, X. H. Li, App. Phys. Lett. **89**, 112113 (2006).

[55] S. S. Lin, H. P. He, Y. F. Lu, Z. Z. Ye, J. Appl. Phys. **106**, 093508 (2009).

[56] Y. Yan, M. M. Al-Jassim, S. Wei, Appl. Phys. Lett. **89**, 181912 (2006).

[57] Z. Huang, H. Ruan, H. Zhang, D. Shi, W. Li, G. Qin, F. Wu, L. Fang, C. Kong, J. Mater. Sci.: Mater. Electron. **30**, 4555 (2019).

[58] A. Tsukazaki, A. Ohtomo, T. Onuma, M. Ohtani, T. Makino, M. Sumiya, K, Ohtani, S. F. Chichibu, S. Fuke, Y. Segawa, H. Ohno, H. Koinuma, M. Kawasaki, Nature Mater. **4**, 42 (2005).

[59] S. Baek, Y. C. Kim, J. Myoung, Appl. Sur. Sci. **480**, 122 (2019).

[60] E. Lee, Y. Kim, Y. Jin, K. J. Chang, Phys. B **308-310**, 912 (2001).

[61] S. H. Park, T. Minegishi, M. Ito, J. S. Park, I. H. Im, J. H. Chang, D. C. Oh, H. J. Ko, M. W. Cho, T. Yao, J. Cryst. Growth **311**, 466 (2009).

[62] N. Ohashi, J. Ceram. Soc. Jpn. **122**, 530 (2014).

[63] K. Ip, M. E. Overberg, Y. W. Heo, D. P. Norton, S. J. Pearton, S. O. Kucheyev, C. Jagadish, J. S. Williams, R. G. Wilson, J. M. Zavada, Appl. Phys. Lett. **81**, 3996 (2002).

[64] Z. Q. Chen, S. Yamamoto, M. Maekawa, A. Kawasuso, X. L. Yuan, T. Sekiguchi, J. Appl. Phys. **94**, 4807 (2003).

[65] P. Trocellier, C. H. Engelmann, J. Radioanal. Nucl. Chem. **100**, 117 (1986).

[66] W. A. Lanford, H. P. Trautvetter, J. F. Ziegler, J. Keller, Appl. Phys. Lett. **28**, 556 (1976).

[67] W. A. Lanford, Nucl. Instrum. Methods Phys. Res. B **66**, 65 (1992).

[68] M. Wilde, K. Fukutani, Sur. Sci. Rep. **69**, 196 (2014).

[69] M. Wilde, S. Ohno, S. Ogura, K. Fukutani, H. Matsuzaki, J. Vis. Exp. **109**, e53452 (2016).

[70] P. A. M. Dirac, Proc. Camb. Phil. Soc. **26**, 361 (1930).

[71] C. D. Anderson, Science **76**, 238 (1932).

[72] R. Krause-Rehberg, H. S. Leipner, Positron Annihilation in Semiconductors Defect Studies, Springer, 1999.

[73] V. S. Shirley, C. M. Baglin, S. Y. F. Chu, J. Zipkin, Table of Isotopes 8th Edition Volume 1, John Wiley and Sons, 1996.

[74] K. Okamoto, K. Tanaka, M. Katsube, O. Sueoka, Y. Ito, Radiat. Phys. Chem. **41**, 497 (1993).

[75] J. V. Olsen, P. Kirkegaard, N. J. Pedersen, M. Eldrup, Phys. Stat. Sol. C **4**, 4004 (2007).

[76] J. M. Campillo-Robles, E. Ogando, F. Plazaola, Sol. Stat. Sci. **14**, 982 (2012).

[77] G. S. Kanda, L. Ravelli, B. Löwe, W. Egger, D. J. Keeble, J. Phys. D: Appl. Phys. **49**, 025305 (2016).

[78] J. Dryzek, E. Dryzek, Acta Phys. Pol. A **110**, 577 (2006).

[79] M. G. Wardle, J. P. Goss, P. R. Briddon, Phys. Rev. B **72**, 155108 (2005).

[80] K. Senthilkumar, M. Subramanian, H. Ebisu, M. Tanemura, Y. Fujita, J. Phys. Chem. C **117**, 4299 (2013).

[81] J. Čížek, M. Vlček, P. Hruška, F. Lukáč, O. Melikhova, W. Anwand, F. Selim, C. Hugenschmidt, W. Egger, J. Phys.: Conf. Series **791**, 012017 (2017).

[82] H. Shimizu, W. Sato, M. Mihara, T. Fujisawa, M. Fukuda, K. Matsuta, App. Rad. Isot. **140**, 224 (2018).

[83] Y. Kang, H. Nahm, S. Han, Sci. Rep. **6**, 35148 (2016).

[84] J. F. Ziegler, J. P. Biersack, M. D. Ziegler, SRIM, the Stopping and Range of Ions in Matter, 2008.

[85] R. C. Arnold, J. Meyer-ter-Vehn, Z. Phys. D Atoms, Molecules and Clusters **9**, 65 (1988).

[86] R. Krause-Rehberg, H. S. Leipner, Appl. Phys. A **64**, 457 (1997).

[87] Y. Wang, M. Muhler, C. Wöll, Phys. Chem. Chem. Phys. **8**, 1521 (2006).

[88] L. Ke, S. C. Lai, J. D. Ye, V. L. Kaixin, S. J. Chua, J. Appl. Phys. **108**, 084502 (2010).

[89] T. Koida, T. Kaneko, H. Shibata, Mater. **10**, 141 (2017).

[90] X. Wang, B. Lu, L. Li, H. Qiu, Chem. Open **7**, 491 (2018).

[91] K. Kodera, I. Kusunoki, S. Shimizu, Bull. Chem. Soc. Jpn. **41**, 1039 (1968).

[92] A. Karbowski, K. Fedus, J. Patyk, Ł. Bujak, K. Służewski, G. Karwasz, Nukleonika **58**, 189 (2013).

[93] J. Tain, H. Zhang, G. Wang, X. Wang, R. Sun, L. Jin, J. Han, Superlattices Microst. **83**, 719 (2015).

Acknowledgements

All of this work was realized by considerable support from many people. I would like to take this opportunity to express my appreciation to them all.

I express the greatest gratitude to Professor Wataru Sato of Kanazawa University for his great support and constructive advice. This paper would have never been accomplished without his encouragement. In addition, he told me how I should be not only as a scientist but also as a human in my student life.

I would like to thank Associate Professor Markus Wilde of The University of Tokyo for his cordial support in the NRA experiments.

I wish to acknowledge valuable discussion with Professor Kohshin Takahashi, Professor Yoshihito Hayashi, Professor Motohiro Mizuno, and Professor Akihiko Yokoyama of Kanazawa University.

I would like to thank the members of Technical Support Center of Kanazawa University for their advice and comments on processing my samples.

I would like to thank Associate Professor Sayaka Komatsuda of Kanazawa University for her kind advice and comments on my work.

I would thank Assistant Professor Mototsugu Mihara, Associate Professor Kensaku Matsuta, Associate Professor Mitsunori Fukuda of Osaka University, and Masashi Ohashi of Kanazawa University for the sample preparation.

I express my gratitude to all members of Radiochemistry Laboratory, Kanazawa University, for their kind support and meaningful discussion in my experiments.

Finally, I thank my father Masato Shimizu for his economical support. I am deeply grateful to my mother Takami Shimizu, my sister Satoko Shimizu, and my wife Asami Shimizu for my peace of mind and for continuous support and encouragement.

List of Publications

Published Papers

[1] H. Shimizu, W. Sato, M. Mihara, T. Fujisawa, M. Fukuda, and K. Matsuta
"Temperature-dependent thermal behavior of impurity hydrogen trapped in vacancy-type defects in single crystal ZnO"
Applied Radiation and Isotopes **140**, 224 (2018)

[2] W. Sato, H. Shimizu, S. Komatsuda, and Y. Ohkubo
"Thermal behavior of In impurities in ZnO"
Journal of Applied Physics **124**, 105101 (2018)

[3] H. Shimizu and W. Sato
"Interactions of intrinsic defects formed in ZnO and their contribution to electric conductivity"
Journal of Applied Physics **126**, 125704 (2019)

[4] W. Sato, S. Komatsuda, H. Shimizu, R. Moriichi, S. Abe, S. Watanabe, S. Komatsu, T. Terai, S. Kawata, and Y. Ohkubo
"Dynamic motion and freezing of polaronic local structures in a colossal-magnetoresistive perovskite manganite $La_{0.7}Ca_{0.3}MnO_3$ detected with radioactive nuclei"
Physical Review B **100**, 184111 (2019)

[5] H. Shimizu, M. Wilde, and Wataru Sato

"Different bound states of impurity hydrogen atoms in hydrothermally grown ZnO detected with nuclear reaction analysis"

Nuclear Instruments and Methods in Physics Research B **467**, 13 (2020)

Bulletins

[1] H. Shimizu, W. Sato, M. Mihara, T. Fujisawa, M. Fukuda, and K. Matsuta

"Observation of vacancy-hydrogen complexes and vacancy-type defects in ZnO by positron annihilation lifetime spectroscopy"

KURRI-EKR-18**,** 20 (2016)